RSS Technical Report 102803 Submitted: October 28, 2003

Sensor Calibration and Ocean Products for TRMM Microwave Radiometer

Final Progress Report for Contract NAS5-00217

October 2000 through September 2003

Principal Investigator: Frank J. Wentz

Submitted to:
Dr. Richard J. Lawrence, COTR
Goddard Space Flight Center
NASA

Remote Sensing Systems
438 First Street, Suite 200, Santa Rosa, CA 95401 (707) 545-2904

Sensor Calibration and Ocean Products for TRMM Microwave Radiometer

Final Progress Report for Contract NAS5-00217

October 2000 through September 2003

Principal Investigator: Frank J. Wentz

Sensor Calibration and Ocean Products for TRMM Microwave Radiometer

Final Progress Report for Contract NAS5-00217

October 2000 through September 2003

Principal Investigator: Frank J. Wentz

1 Introduction

During the three years of funding, we have carefully corrected for two sensor/platform problems, developed a physically based retrieval algorithm to calculate SST, wind speed, water vapor, cloud liquid water and rain rates, validated these variables, and demonstrated that satellite microwave radiometers can provide very accurate SST retrievals through clouds. Prior to this, there was doubt by some scientists that the technique of microwave SST retrieval from satellites is a viable option. We think we have put these concerns to rest, and look forward to making microwave SST's a standard component of the Earth science data sets. Our TMI SSTs were featured on several network news broadcasts and were reported in Science magazine.

Additionally, we have developed a SST algorithm for VIRS to facilitate IR/MW inter-comparisons and completed research into diurnal cycles and air-sea interactions.

As outlined in this final report, our work involved:

(1) Sensor or platform problems:
   a. Studies of TMI Level 1 Calibration problems (the graphite antenna correction)
   b. Correction for errors in the attitude control system

(2) Fine tuning the Ocean Algorithm
   a. TMI V02: Fine tuning the sea-surface emissivity model
   b. TMI V03

(3) Validation of the SST and wind speeds
   a. In situ validation
   b. Satellite SST Inter-comparisons
   c. Implementing a near real time validation to monitor any unexpected problems
   d. TMI Wind Speed Validation

(4) Diurnal Warming in SSTs
   a. Diurnal variability: satellite and in situ
   b. Diurnal variability: IR and MW SSTs
   c. Development of an empirical model for TMI
   d. Comparisons to diurnal warming measured by AVHRR
   e. Comparison to diurnal warming measured by moored buoys

(5) VIRS SST algorithm
   a. IR cloud detection
   b. Testing different algorithms
   c. Comparisons between the MW and IR retrievals

(6) Research applications

a. Tropical Instability Waves
b. Testing TMI SSTs in NCEP OI SSTs
c. Tropical cyclones
    i. Intensity forecasting
    ii. Cold wake climatology

2 Sensor or platform problems

The TRMM TMI products have two separate corrections made, first a correction for oxidization of the vapor deposited aluminum on the antenna and, later in the mission, a correction for increased attitude control errors. These are both discussed below.

2.1 Studies of TMI Level 1 Calibration problems (the graphite antenna correction)

This calibration was an essential precursor to subsequent use of the TMI data for meteorological and oceanographic studies. The calibration research used three independent methods to examine two distinct types of calibration error. The three analytical tools were regression of long-term data sets of ocean observations, comparison to co-located SSM/I observations, and pitch-over platform maneuvers during which TMI viewed deep space.

The long-term ocean data was examined for the entire year of 1998, as well as the entire year of 1999. The results of the examinations for both years were almost identical. Through this investigation, we carefully quantified consistent along-scan biases to each of the channels. These along-scan biases were extremely consistent for any one channel, although they differed dramatically from one channel to another. The along-scan biases were confirmed during the pitch-over maneuvers. One interesting aspect of the along-scan bias was that it was very nearly the same when viewing the ocean as it was when viewing cold space. In other words, it appears to be mostly independent of the actual scene temperature.

The second type of bias was an absolute offset (independent of scan position). In other words, the observed temperatures were warmer than they should have been. This offset became evident through comparison to SSM/I observations, as well as through the pitch-over maneuver. The nature of this offset was that it was small at high temperatures, and increased as the scene temperature decreased.

We were able to outline several possible explanations for each of these error types. Whatever the exact mechanical explanation for these biases, they were each consistent, and could consequently be corrected. As a result of our calibration work, we were able to produce correction factors that have now been incorporated into the latest version (version 5) of the official TMI brightness temperature product.

We continued working on this problem, and finally, evidence pointed to the vapor-deposited aluminum on the TMI antenna. It was entirely oxidized by atomic oxygen shortly after launch. As a result, TMI has a graphite antenna, with a reflectivity of 96%.

We developed an improved method of determining the temperature of the graphite antenna. Temperature variations in the antenna produce a unique spectral/polarization signature in the T_B's. As a result, the temperature of the antenna can be retrieved like any other parameter from the T_B's. The bad news is that the retrieval is very noisy for individual observations. The good new is that the temperature is fairly constant over 50 scans, and hence the retrievals can be averaged to reduce the noise. The retrievals can be averaged over 50 scans and also over 3 days since the same heating cycle occurs during each orbit. These very large averages reduce the noise considerably. We also use the on-board thermistors for additional information on the temperature of the antenna. Figure 1 shows the improvement that was realized with this new method. The green line shows the results from the original algorithm (version 1) and the blue line shows the results of the new algorithm (version 2). The annual signal in SST is clearly the dominant harmonic, but there are also high frequency peaks, due to yaw maneuvers, apparent in the green line (V01). For the V02 algorithm, these peaks are significantly reduced (blue line).

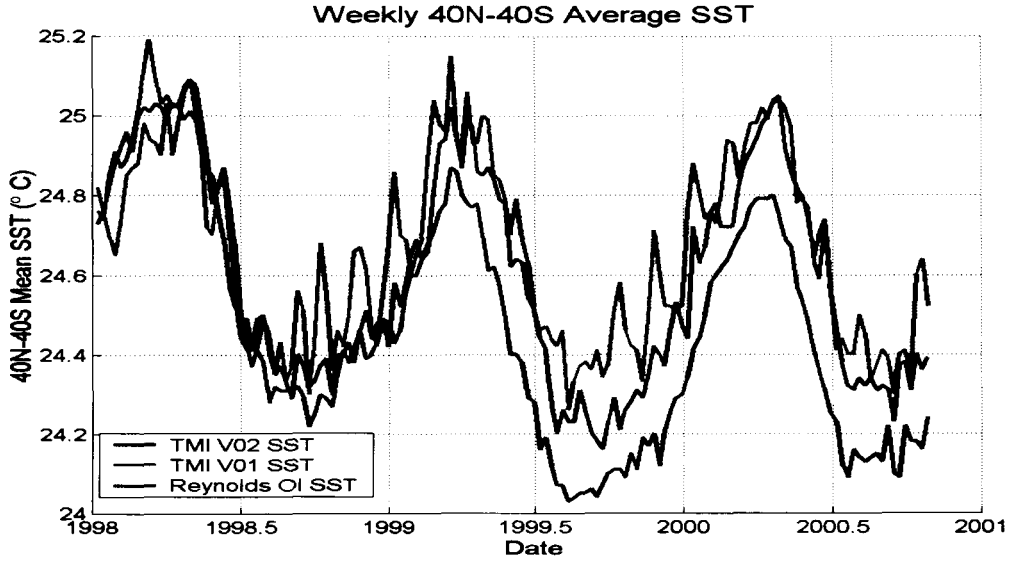

Figure 1. Weekly 40N - 40S average SST for TMI Version 1 algorithm, TMI Version 2 algorithm, and Reynolds OI SST.

2.2 Correction for errors in the attitude control system

The August-September 2001 boost of the TRMM satellite altitude rendered the primary sensor for onboard attitude control determination, the Earth horizon sensor, unusable. Post-boost, the satellite attitude has been determined by a Kalman filter utilizing the magnetometer, sun sensor, and gyros. The Kalman filter's ability to determine attitude control, while still within specifications, is less accurate than the Earth horizon sensor. This increased uncertainty in determination of attitude control has introduced small errors in reported platform roll, causing errors in calculation of geolocation and incidence angle. Due to the incidence angle dependence of the sea-

surface emissivity, the TMI sea-surface temperature (SST) and wind speed algorithms are extremely sensitive to errors in incidence angle. Post-boost roll errors were immediately noticeable in the SST retrievals. Figure 2 shows the Version-2 and Version-3 TMI SSTs on September 28, 2001, a day with large ACS errors. The top panel is the uncorrected Version-2 TMI SSTs while the bottom panels shows the corrected Version-3 TMI SSTs. Virtually all roll error is removed from the bottom panel.

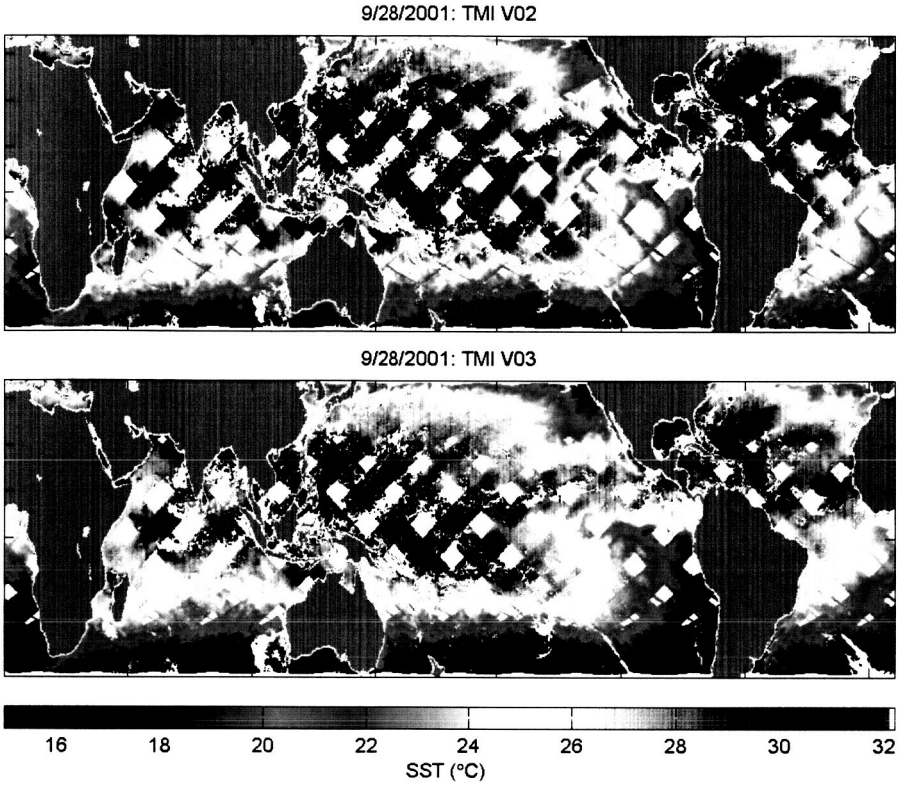

Figure 2. The top image shows the mean TMI - Reynolds OI SST for all orbits on September 28, 2001 before making the roll/pitch correction. Systematic cross-swath errors in the SST retrievals are obvious. The bottom image shows the results after making the roll/pitch correction. The cross-swath errors have been eliminated.

At the Fort Collins meeting, John Kwiatkowski presented an estimate of the roll error derived from analysis of the Precipitation Radar (PR) retrievals. He kindly provided us with this data, so we could try to correct the errors in incidence angle affecting the TMI SST and wind speed calculations. The PR correction can only estimate roll error and it is very possible there are errors in pitch measurement also.

We investigated several possible corrections. Using the difference between the Reynolds OI SST and TMI SST, we were able to very successfully model ACS errors using the TMI SSTs, but we also investigated using the PR radar estimate of roll error. Our decision to use the TMI SST estimate was based on our ability to accurately reproduce the PR estimate of roll error and our ability to estimate pitch errors in addition to roll errors. In addition using TMI rather than the PR allows us to make roll and pitch corrections for the entire TRMM mission.

The Reynolds OI SST is a blended analysis. Although it does have errors, it does not have errors with orbital characteristics like the TMI ACS error. This allows us to use the difference, TMI – OI SST, to model roll and pitch errors. We developed the following model to describe roll and pitch errors. The difference of the TMI SST retrieval minus the Reynolds retrieval, which is denoted by ΔSST is assumed to be due to the error $\Delta\theta$ in specifying the incidence angle θ

$$\Delta SST = \frac{\partial SST_{retrieval}}{\partial \theta}\Delta\theta$$

where the sensitivity of the SST retrieval to a change in θ is found by doing the retrieval at two different θ bracketing the specified θ. The error in incidence angle is related to the roll error Δr and the pitch error Δp by the following relationships:

$$\Delta\theta = \frac{\partial\theta}{\partial r}\Delta r + \frac{\partial\theta}{\partial p}\Delta p$$

$$\frac{\partial\theta}{\partial r} = \left(\sin\alpha + 1.1993\sin^3\alpha\right)\left[0.52085 + 0.0001988\left(h - 375\right)\right]$$

$$\frac{\partial\theta}{\partial p} = \left(\cos\alpha + 1.1993\cos^3\alpha\right)\left[0.52085 + 0.0001988\left(h - 375\right)\right]$$

where θ is the TMI scan angle (θ=0 is looking directly forward) and h is the satellite altitude in kilometers. These relationships are very accurate approximations for the actual scan/spacecraft geometry. The roll error is assumed to vary as a first order harmonic of the orbital position ϕ (ϕ = 0 is the start of a TRMM orbit at its most southerly point). We found no significant orbital variation in the pitch error, so it is simply modeled as a single value for a given orbit.

$$\Delta r = c_1 + c_2\cos\phi + c_3\sin\phi$$

$$\Delta p = c_4$$

The regression coefficients c_1 through c_4 are found by standard least squares. A set of coefficients is found for each orbit. The data used for each orbit consists of 15 orbits centered on the specified orbit. Thus although the coefficients are provided for each orbit, their intrinsic temporal resolution is one day.

The coefficients were estimated from December 1997 through March 2002. Figure 3 shows the estimates of roll error from the PR radar (red), Version-2 TMI SSTs (black), and Version-3 (corrected) TMI SSTs (blue). The top two figures show the roll error amplitude = $\sqrt{c_2^2 + c_3^2}$ and phase = ArcTan(c_3,c_2) after the orbital boost. Errors in SST reached a maximum of 3.2°C during this period. As a check for both the PR and TMI error estimates, the TMI estimate of amplitude and phase are plotted alongside the estimates from the PR in Figure 3. These independent calculations of roll errors agreed extremely well, indicating both methodologies can accurately estimate roll error. Also shown in Figure 3 is the residual roll error inferred from the corrected SSTs (version 3), verifying that the errors have been nearly completely removed. The bottom two panels in Figure 3 show the roll error amplitudes and phases since launch. Small ACS errors are

apparent before the orbital boost. We were able to correct the entire time series for ACS errors in the Version-3 SSTs.

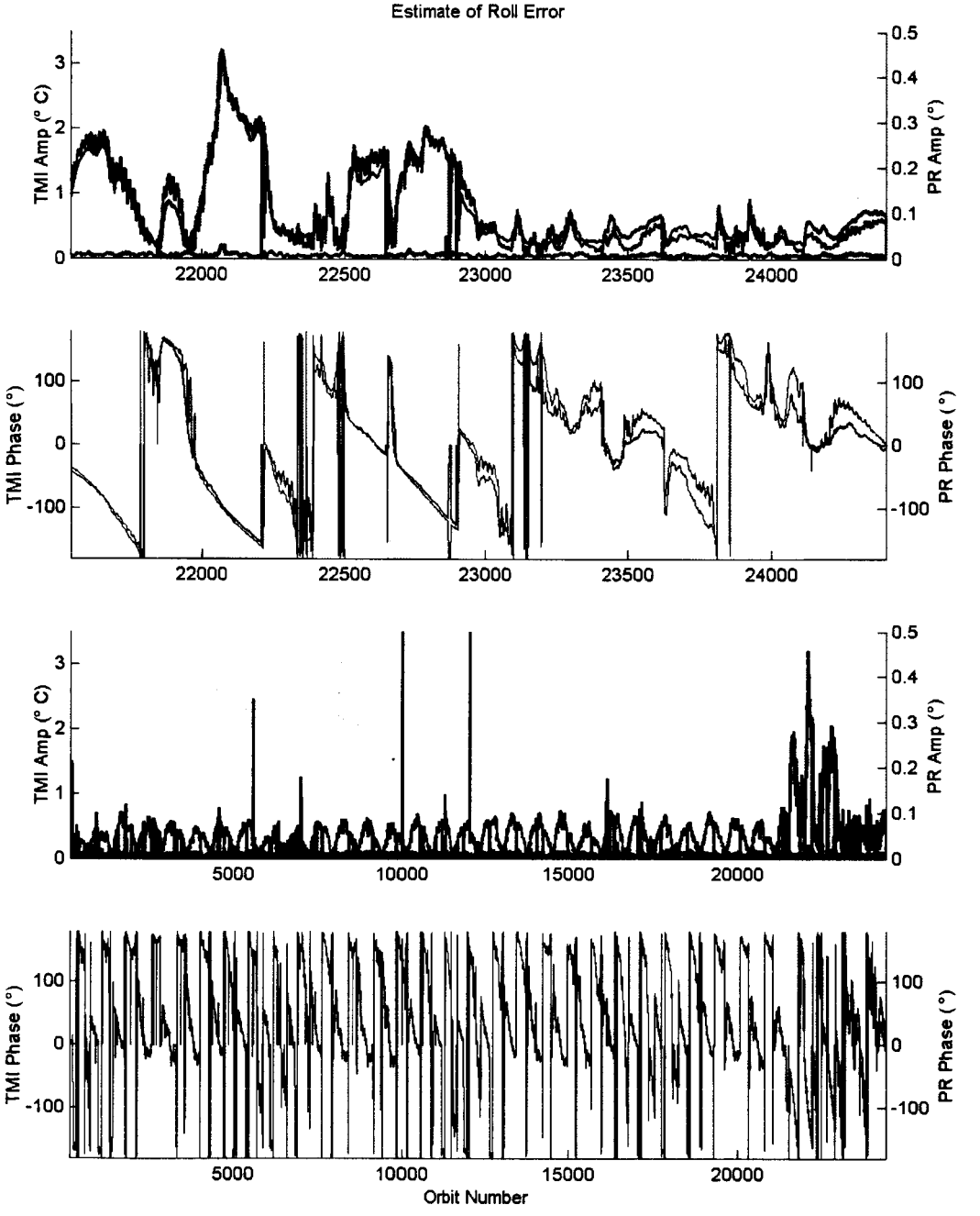

Figure 3. The top two frames show the amplitude and phase of the TRMM roll error after the August 2001 orbital boost. The red curve shows the results from the Precipitation Radar (PR), and the back curve shows the results derived from the TMI SST retrievals. The blue curve shows the residual roll error after correction. The bottom two frames are the same as the top two except that the time period is for the entire TRMM mission. The green/white panels in the background of all figures indicate 0° and 180° yaw.

On March 23, 2002 we reprocessed the post-boost dataset and put TMI_V03 online. We only added a correction for the orbit boost for the August 2001 – March 2002 data since we were told that the Kalman filter was now working and initial results indicated the ACS errors to be quite small. We have recently re-visited the problem and found that an on-going ACS error correction must be developed and implemented into our near-realtime processing. Figure 4 shows the TMI SST calculation of pitch error for Version 3 (blue) and Version 2 (red). Before the orbital boost, pitch errors were very small, but after the boost they became extremely large. We corrected for them (shown by the flat blue line) until orbit 24500 where the problem seemed smaller for a short time. The figure clearly shows that it is still a problem that needs to be addressed.

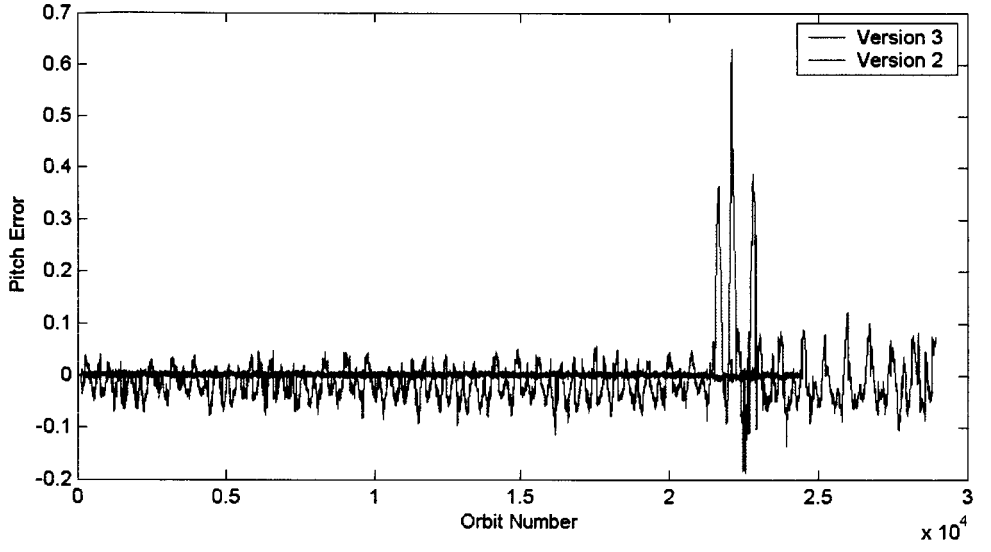

Figure 4. Pitch Errors in TMI SSTs.

Based on the errors still apparent after the initial reprocessing, we developed a real time correction for pitch/roll errors and reprocessed the data. (TMI V03a). This on-going correction corrects for the pitch/roll errors seen in Figure 4.

3 Fine tuning the Ocean Algorithm

3.1 TMI V02: Fine tuning the sea-surface emissivity model

The TMI V01 algorithm was a hybrid of regression algorithms and RTM-T_B matching algorithms. Based on new results coming from our AMSR investigation, it appears that retrieval algorithms based on 2-stage regressions perform as good as (or possibly better) than the RTM-T_B matching algorithms. Since we want the TMI ocean algorithm to be a surrogate for AMSR, we decided to revise the TMI algorithm, substituting the 2-stage regressions for the RTM-T_B matching algorithms. There were a number of other improvements as well, including the improved method for handling the graphite antenna and the removal of the reliance on climatology (see next paragraph). The new algorithm

is called V02. The V02 algorithm is the same in both structure and functionality as the AMSR algorithm. By having common data processing routines that can accommodate both AMSR and TMI, we can more fully test the AMSR algorithm using TMI observations. In addition, we will have greater confidence that the AMSR algorithm will perform similarly to the TMI algorithm given that the new algorithms have nearly the same form.

One problem addressed in the V02 algorithm relates to the influence of climatology on the SST retrieval. The Version-1 TMI algorithm uses climatology SST to specify air temperature. As a result, the TMI SST retrievals are, to a small degree, tied to the climatology value. We now have nearly three years of TMI SST retrievals, and we can determine TMI's capability to track small inter-annual variability in the SST. The TMI time series begins at the height of the 1997 El Nino, and then sees the rapid cooling that begins in early 1998. We compared the TMI tropical time series from December 1997 through September 2000 with the TOGA-TAO equatorial buoy array. It appears that the TMI time series is not fully tracking the cooling event. TMI underestimates the cooling trend by about 10%. We have now traced this problem back to a small problem with the retrieval algorithm. The retrieval algorithm uses a climate SST to specify air temperature, and hence the SST retrievals have a small dependence on the value of the climate SST. A 1°C change in the climate SST produces about a 0.1°C change in the retrieved SST (i.e., a 10% effect). Thus the SST retrieval is, to a small degree, tied to a static climate value, and hence does not fully track the true climate signal. The new 2-stage physical regression algorithm that we are currently implementing for TMI (and AMSR) does not use a climate SST for the SST retrieval, so we hope this problem will go away when the new algorithm is implemented and tested.

3.2 TMI V03

Our initial ocean algorithm (TMI V02) required fine-tuning based on validation results. TMI V03 was released with a new retrieval algorithm. These new algorithms provide better agreement with scatterometer wind speeds. Systematic errors and crosstalk in the SST and wind retrievals have also been reduced. Another feature of the new algorithms is that they have a high degree of commonality with those algorithms that will be used for the SSM/I reprocessing, and for the upcoming AMSR and SSM/IS missions. Also, the V02 algorithm had a bug that caused extremely high rain rates to be inadvertently flagged as missing data. This problem is corrected in V03.

After a closer look at the systematic wind errors using the TMI and QuikScat comparisons a 2-dimensional (wind and SST) histogram of the wind differences was produced. These histograms revealed that the wind difference is jointly correlated with both wind and SST. Earlier analyses, which considered wind and SST separately, failed to show significant correlation. However, when working in terms of a joint SST-wind correlation, an appreciable correlation is obtained. It appears that the wind-induced sea-surface emissivity should be modeled as both a function of SST and wind.

To correct the wind bias problem, we re-derived the sea-surface emissivity model. The TMI T_B observations are first transformed to emissivity values, and then these emissivities are stratified into SST and wind speed bins. The SST comes from Reynolds weekly values, and the wind speed comes from collocated QuikScat observations. The

new wind-induced emissivity model shows more dependence on SST than did the previous model. The coefficients for the retrieval algorithm were then recomputed using the new emissivity model. These new results were included in TMI V03 and validation is discussed in the next section.

4 Validation of the SST and wind speeds

Validation of the TMI SST was a major focus of this investigation. We previously reported surprisingly large differences between the Reynolds Optimum Interpolated SST (OI SST) and TMI SSTs exist in regions with sparse in-situ retrievals, high atmospheric water vapor content, and persistent clouds. The NCEP Reynolds OI SST product blends AVHRR SSTs with in-situ retrievals from moored buoys, ships, and drifting buoys. The in-situ retrievals are used to calculate a bias correction for possible aerosol and vapor attenuation errors present in the AVHRR SSTs. We continued this validation by focusing on three-way comparsions: TMI, OI and buoy SST comparisons

4.1 In situ validation

The buoy comparisons highlight the problems with comparing point measurements to 50-km averages. We began with an examination of individual buoy time series, which revealed considerable variability between moorings. Many show excellent agreement, but some show seasonal/intra-seasonal differences, mean offsets, and trends. Evidence of small scale SST variability for individual buoys is shown with a time series from three TAO buoys (Figure 5). The time series shown are of the weekly average buoy SST, TMI SST, and Reynolds' OI SST.

Figure 5A, TAO/TRITON buoy 51309, reveals TMI to be cooler than either the buoy or OI SSTs. It also shows significantly more variance. Both the lower temperature and the larger variance are reflected in AVHRR SSTs (not shown), indicating that the local field the buoy is measuring is not indicative of larger (18 km or 50 km) averages of the AVHRR and TMI retrievals. This particular buoy is located in the ITCZ, a cloudy region with few AVHRR retrievals. Since there is little AVHRR data for this buoy, the OI SST gives a very high weight to the buoy value, which is very apparent in Figure 5A by the close agreement between the buoy and the OI SST.

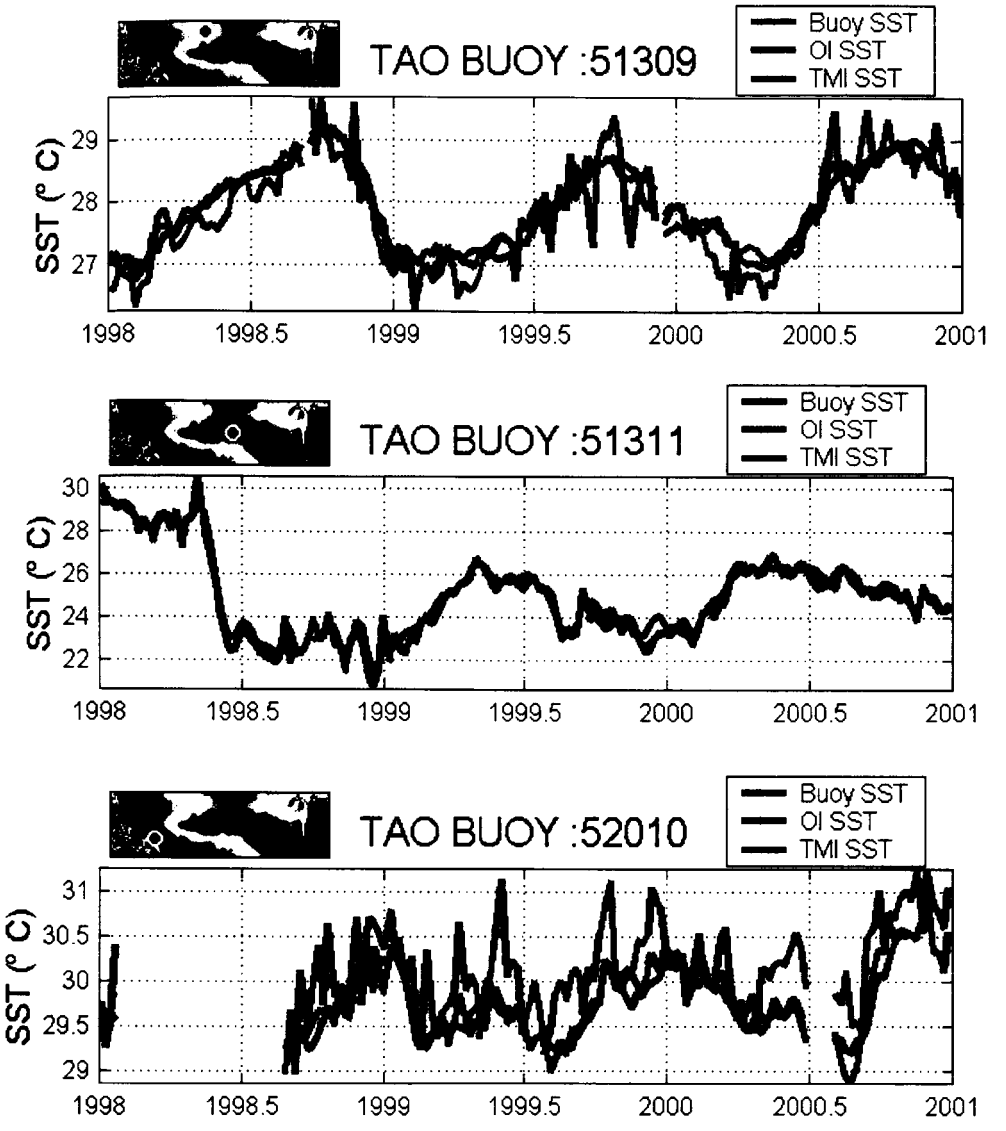

Figure 5. Time series of buoy SST (blue), Reynolds OI SST (red), and TMI SST (green). A map at the top left of each panel shows the buoy location. SSTs were collocated to within 25 km and 1 hour. Weekly averages were calculated from the collocated retrievals.

TAO buoy 51311, located in the center of the Equatorial cold tongue, is shown in Figure 5B. As expected, for this region with low temporal/spatial variability, both the OI and TMI SSTs are tracking it very accurately.

A third comparison, Figure 5C, shows TAO buoy 52010, located near the coast of New Guinea in a region with extremely high atmospheric water vapor, persistent cloud, and many small islands or atolls. Similar to Figure 5A, the high variability witnessed in TMI is also reflected in AVHRR retrievals, when they are available. TMI is on average warmer than the buoy SST during the summer months. In contrast, AVHRR retrievals all exhibit a cool bias in this region, likely due to the extremely high water vapor.

Comparison between OI and buoys are somewhat misleading when viewed as a validation of IR SSTs since OI SST ingests the buoys into the analyses. The OI SST should follow the buoys very well; differences may be due to sub-pixel SST variability. The variability between individual buoys underscores the necessity for averaging over many buoys to minimize individual buoy biases when calculating statistics.

Table 1 shows the mean residual (TMI – buoy SST) and standard deviations calculated from 3 years of collocations to the RSS buoy dataset. The small errors and standard deviations testify to the accuracy of microwave SST retrievals. As expected, there are larger biases and standard deviations for the NDBC array. The larger standard deviations are likely due to the small-scale temporal and spatial variability common to the NDBC buoy locations. The standard deviations for the TAO and PIRATA collocations (0.53°C and 0.50°C respectively) agree well with the expected algorithm accuracy, 0.5°C. Notably, TMI does not include buoy retrievals in the development of the retrieval algorithm, so accuracies estimated in this manner may be confidently extended globally.

Table 1. Comparison between TMI and buoy SST

Buoy Array	Collocations	Mean	STD
TAO	42633	-0.06	0.53
PIRATA	4415	0.05	0.50
NDBC	20663	0.28	0.82

4.2 Satellite SST Inter-comparisons

The 3-year TMI data set validation results for the SST indicated good performance. The SSTs accurately tracked the El Nino-to-La Nina cooling trend, showing nearly (within 0.1 C) the same trend as reported by the TAO array of buoys, as is shown in Figure 6. Thus, as we expected, the problem with using the climatology SST in the V01 algorithm has gone away.

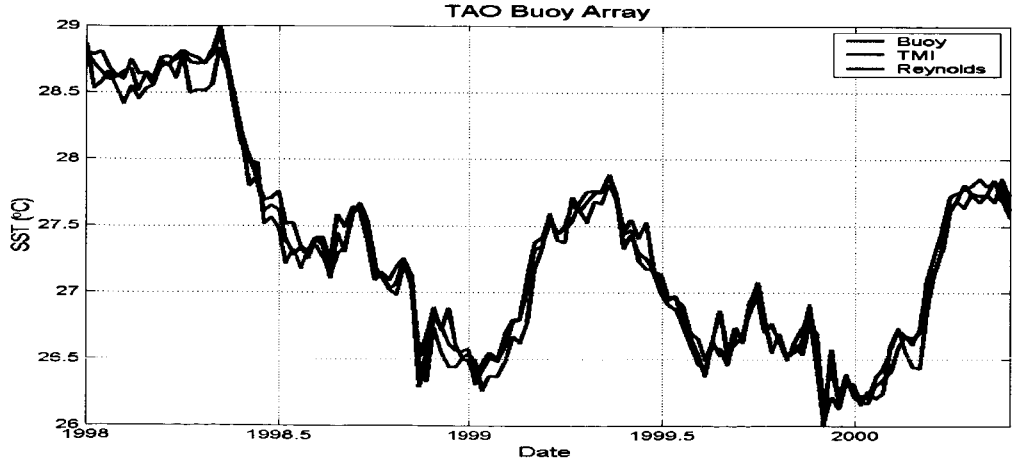

Figure 6. Time series of SST from TAO buoys, TMI, and Reynolds' OI product.

Further SST validation involved creating a global array of time series of Reynolds and TMI SST. The annual and semi-annual signals dominate the SSTs, so each time series was fit with a multiple linear regression that included terms to account for annual and semi-annual harmonics. The fits were calculated using data from 1999 and 2000 since the La Nina signal dominated the 1998 SSTs. Calculations of the trend that included 1998 resulted in a clear La Nina cooling dominating the tropics. Global mean differences with trends, annual, and semi-annual harmonics removed are shown in Figure 7.

Figure 7A and 7C are very similar. The difference, which is shown in Figure 7B, is largest and positive (TMI warmer than Reynolds) in the southern hemisphere, regions virtually devoid of in-situ measurements. The results shown above are consistent with buoy residuals. The TAO array biases (TMI – Buoy SST) are small and slightly negative. The large positive region in the southern Indian Ocean is an area with high winds much of the year. The biases in the Pacific and Atlantic are puzzling. It is difficult to ascribe error to either TMI or Reynolds, as independent retrievals (i.e., in situ) are not available in these regions. Drifters are available, but their quality is not adequate for measuring these small errors. VIRS-TMI retrievals may result in a better understanding of this problem.

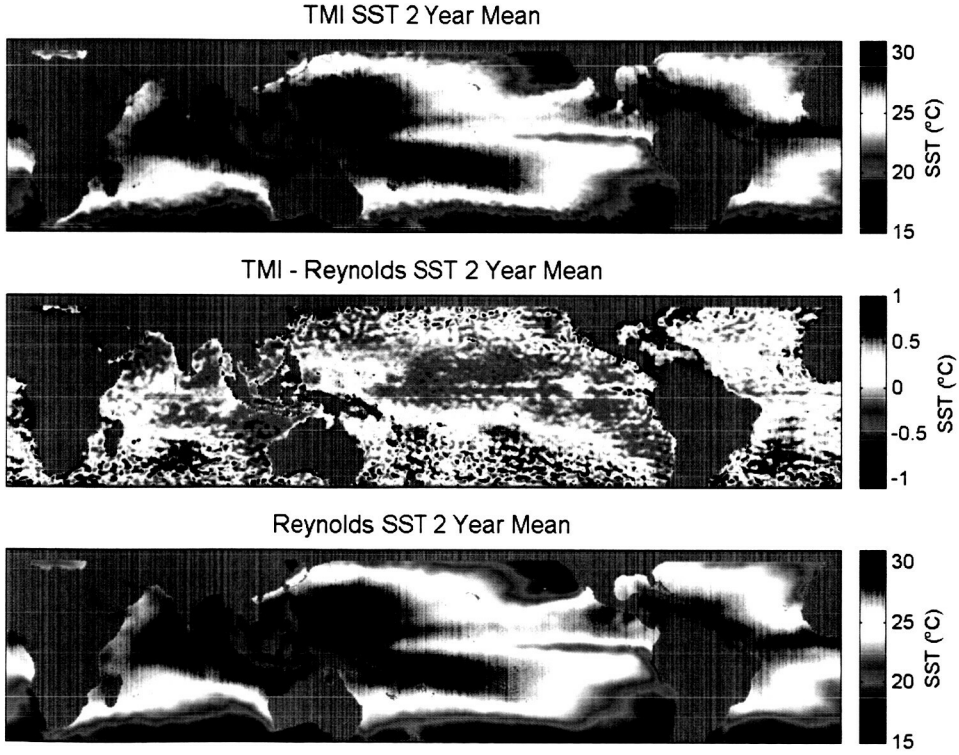

Figure 7. A: TMI 2 year global average SST. B: TMI - Reynolds 2 year average difference. C: Reynolds 2 year mean SST.

4.3 Implementing a near real time validation to monitor any unexpected problems

Our experience with the orbital boost error discussed above led us to develop a real-time validation of the TMI SSTs as a monitoring tool. We post these validation results in

near real-time (NRT) on our website. This allows RSS and data users to easily keep track of biases in the dataset. Near real-time in situ observations are downloaded daily from the Global Ocean Data Assimilation Experiment (GODAE) Monterey server, which is sponsored by the Office of Naval Research (ONR) and hosted by the Fleet Numerical Meteorology and Oceanography Center (FNMOC). These observations are obtained by FNMOC from the GTS and processed for the GODAE server. Observations from ship engine room intake, fixed buoy, drifting buoy, ship hull sensors, and CMAN stations are included in the dataset. The http://www.usgodae.fnmoc.navy.mil website has the complete SURFOBS dataset and a detailed description.

To perform the comparisons with TMI, in situ observations are collocated with the closest TMI SST observations (within 25 kilometers; to the nearest TMI observation time). The complete collocated dataset is available online in text format, but for a quick understanding of the NRT error statistics, the previous 50-day bias and standard deviation are plotted daily. All figures and data are all available in near real-time from www.remss.com. Figure 8 shows the locations of all in situ observations for most recently computed day. Figures 9 shows the mean bias and standard deviation between TMI and in situ data from the GTS.

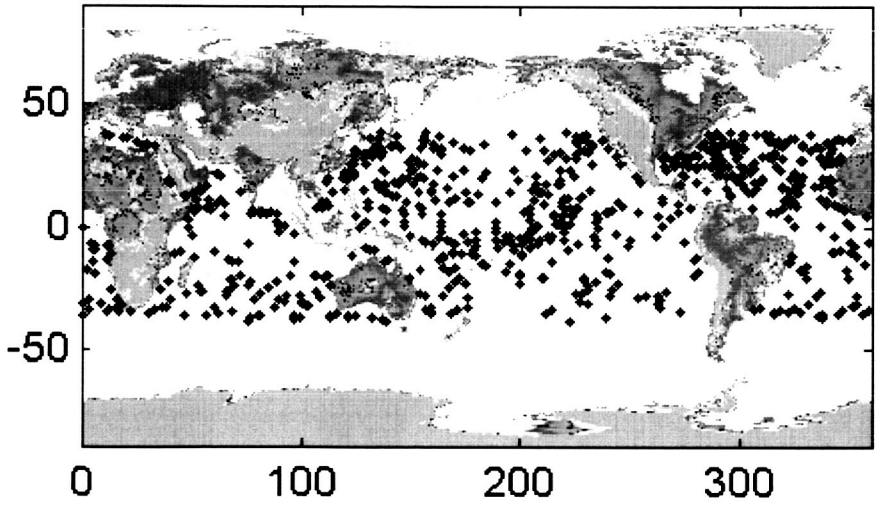

Figure 8. In Situ Data Collocations for the Most Recently Completed Day

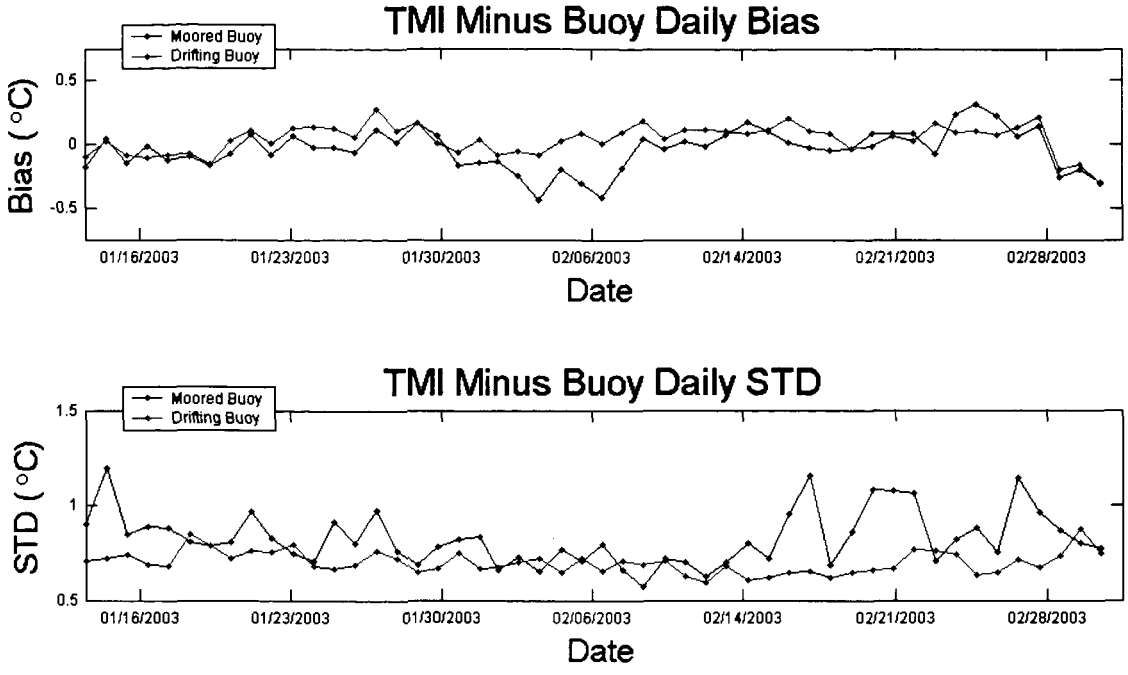

Figure 9. The mean daily bias and standard deviation of TMI SSTs minus in situ SSTs.

Also available at the website is a file contains daily summary statistics from August 1998 to the current time for buoys as well as ship based measurements. The start date coincides with GODAE data availability. The ship-based measurements have a significantly higher degree of variability than buoys and are not shown in Figure 9.

Additional validation is performed using the NCEP OI global, weekly 1°x1° SST (commonly referred to as Reynolds SST) product. It is a bias adjusted optimum interpolation of AVHRR SSTs and in situ observations following Reynolds and Smith (1994). The previous week's analysis is available every Monday from www.emc.ncep.noaa.gov/research/cmb/sst_analysis. To perform this comparison with TMI, Reynolds weekly fields are interpolated to the TMI observation time. TMI observations between 6 AM and 6 PM local time are considered day; TMI observations between 6 PM and 6 AM local time are considered night. The complete collocated dataset is available below in text format, but for a quick understanding of the NRT error statistics, the previous 50-day bias and standard deviation are plotted in Figure 10. At our website we have made available a file containing the daily summary statistics from December 1997 to the current time.

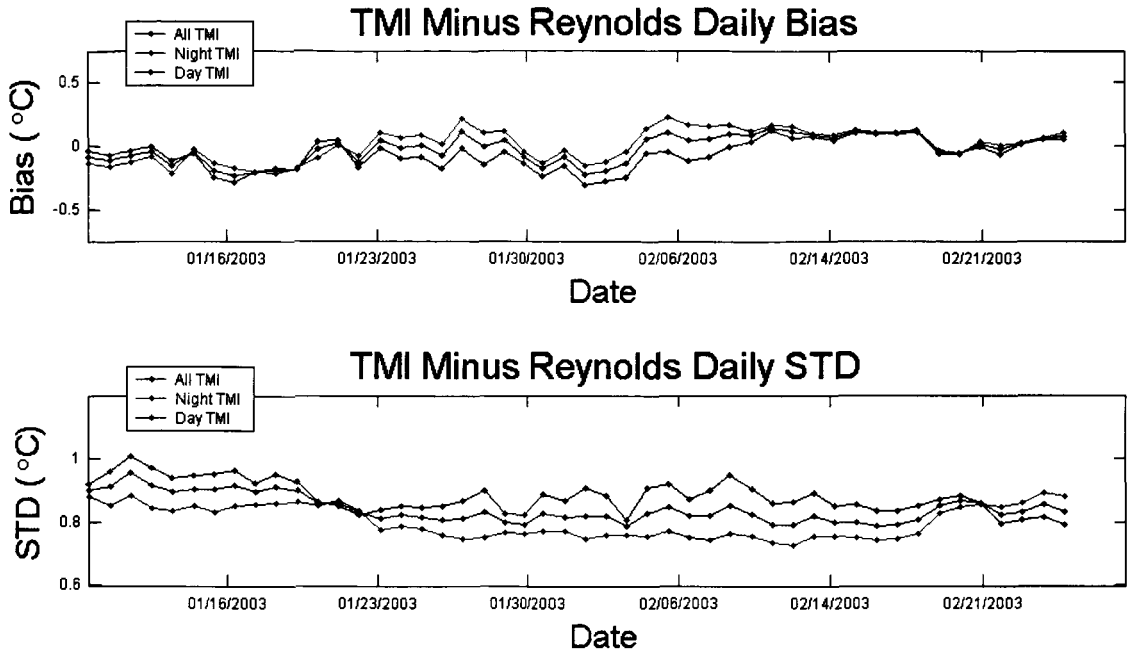

Figure 10. The TMI minus Reynolds OI SST daily bias and standard deviation.

4.4 TMI Wind speed validation

The wind speed validation of the V01 algorithm revealed regional biases between the TMI winds and the QuikScat scatterometer winds. We have known for some time that regional biases exist between active and passive retrievals of wind speed. These were shown by earlier SSM/I versus QuikScat comparisons (see the top of Figure 11). The appearance of these same biases in the TMI comparisons verified that there was something fundamental in the radiative transfer model that caused the problem. We determined the emissivity model used in radiometer data processing needed to be updated.

Once the emissivity model was updated and reprocessing of the TMI data was performed, the TMI versus QuikScat wind speed comparisons were redone. The bottom panel of Figure 11 shows the TMI-QuikScat wind speed difference using the new emissivity model. The regional wind biases are now much smaller: about ± 0.5 m/s rather than ±1.5 m/s with the old model. These results confirm that the long-standing difference between wind speed retrievals from active versus passive microwave sensors is mostly due to the sea-surface emissivity model being slightly incorrect.

Recent validation of the V03 algorithm 11GHz TMI wind speeds with QuikSCAT data showed a bias of 0.34 m/s with a standard deviation of 0.64 m/s for a one-year sample consisting of over 10 million matchups. The corresponding wind speed difference map, shown in Figure 12, highlights that 11GHz channel winds behave differently than 37 GHz channel winds (shown in the bottom panel of Figure 11) in that the regional biases are even further reduced to less than +/-0.5 m/s.

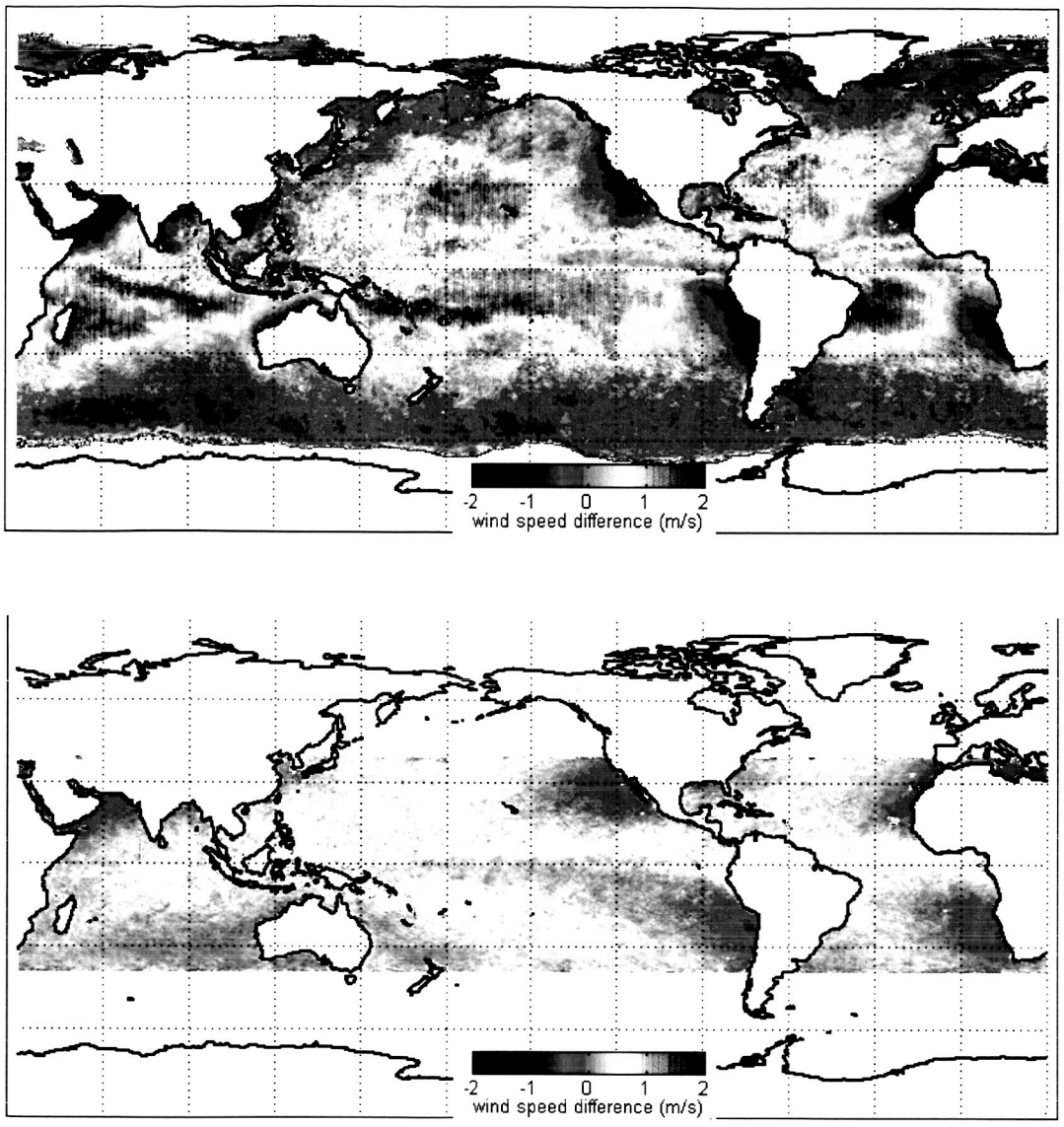

Figure 11. Wind speed differences between microwave radiometers and microwave scatterometers. The top panel shows the SSM/I minus QuikScat wind speed difference resulting from the old emissivity model. The bottom panel shows the TMI minus QuikScat wind speed difference resulting from the new emissivity model. The regional biases are now about ±0.5 m/s as compared to ±1.5 m/s for the old model. These figures are an averaged from July 1999 to September 2000.

5 Diurnal Warming in SSTs

The upper ocean is usually well mixed by wind waves, but during the daytime low wind speeds and increased solar insolation can result in strong thermal stratification of the top few meters, leading to significant warming at the surface. At lower wind speeds, the surface temperature can warm up to 3°C. The water temperature at 1-meter depth,

typically used as boundary condition by climate models, is within this warm layer. This temperature has a diurnal warming that peaks in the afternoon, slightly later than the peak of the surface temperature observed by Infrared (IR) and microwave (MW) satellite retrievals.

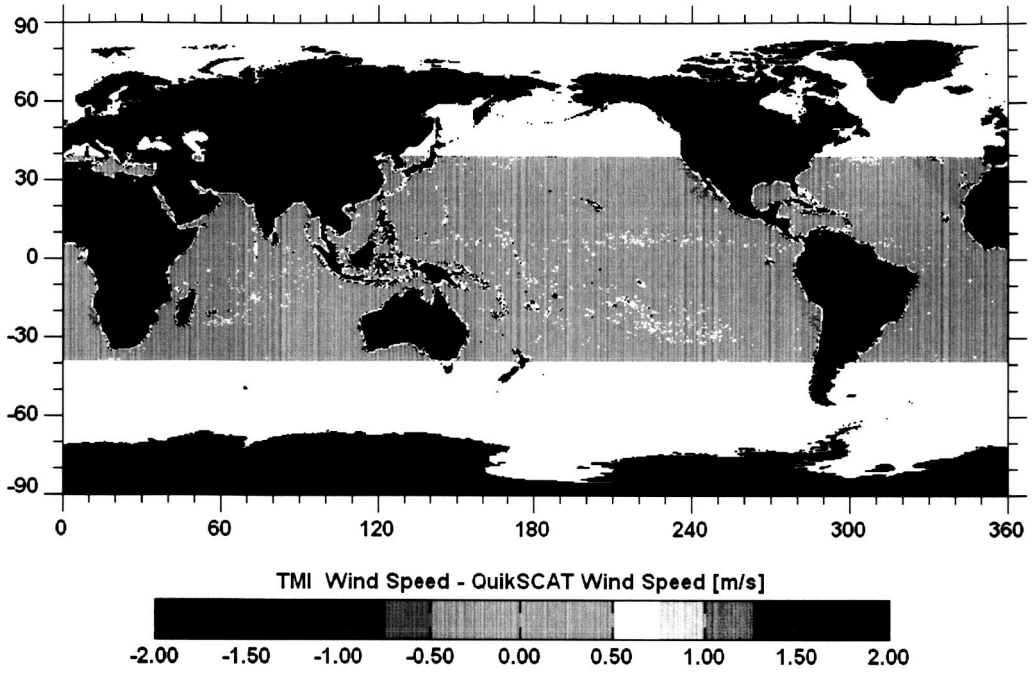

Figure 12. TMI – QuikSCAT wind speed difference map for July 2002 through June 2003. Regional biases seen in Figure 11 are further reduced by using the 11GHz TMI wind speed instead of the 37 GHz wind speed in the comparison.

In the past, diurnal effects have been under-estimated or ignored by the satellite SST community. SST is usually defined as a skin (the temperature of the top few microns) or bulk (the temperature at a depth of one meter) measurements. The skin SST controls air-sea heat flux (both sensible and latent) and the net longwave flux, while the bulk SST is a more stable average of mixed layer temperature, useful for oceanographic and climate research. The diurnal warming of SSTs should be taken into account when using observed data for climate models, as it can affect the calculation of air-sea flux. Climate quality SST records that include satellite retrievals must remove the diurnal signal to provide a meaningful time series, while SSTs utilized by NWP models and coupled models need information about the magnitude and distribution of diurnal warming. For example, the depth of the mixed layer in the western Tropical Pacific, which is related to ENSO events, can be affected by the strong diurnal signal in that region. On a much shorter time scale, the atmospheric convection in that region may be significantly affected by the oceanic diurnal cycle.

These applications all require a global SST, which in the future will likely be a combination of multi-sensor SSTs including both infrared and microwave retrievals.

Blending SSTs from satellites with different local observation times requires accurate accounting of diurnal amplitudes for each type of retrieval. We have begun a study to estimate the phase and magnitude of diurnal warming present in both satellite and in situ retrievals, along with associated error estimates.

Understanding the diurnal cycle is also extremely important for calculating errors in the satellite SSTs, which requires validation through cross-comparison with *in situ* and other satellite data. Validation of the satellite SSTs is primarily through *in situ* collocations. While a number of collocations come from skin radiometers mounted on research vessels or buoys (MOBY), the majority of *in situ* measurements are from moored buoy platforms which measure at 1m depth, or drifters which measure at 5m. Accurate validation of satellite retrievals must account for de-coupling of the surface skin layer with *in situ* measurements at depth, and for the difference between satellite measurements made at different local times during conditions conducive to diurnal warming.

5.1 Diurnal Variability: satellite and in situ

To examine the satellite and *in situ* diurnal cycles, we compared 3 years of SSTs from TMI and two buoy datasets, the NDBC and TAO. We subtracted Reynolds OI SSTs, a weekly product with no diurnal signal. This allows the residuals to be examined for mean diurnal variability. The four plots in Figure 13 show the results for two cases: (1) only data with wind speeds between 6 and 10 m/s during the day, when enhanced vertical mixing in the upper ocean quickly erodes any diurnal warming present at the surface, and (2) only data with wind speeds less than 3 m/s, when thermal stratification in the upper ocean layers is strong and the diurnal warming can be significant.

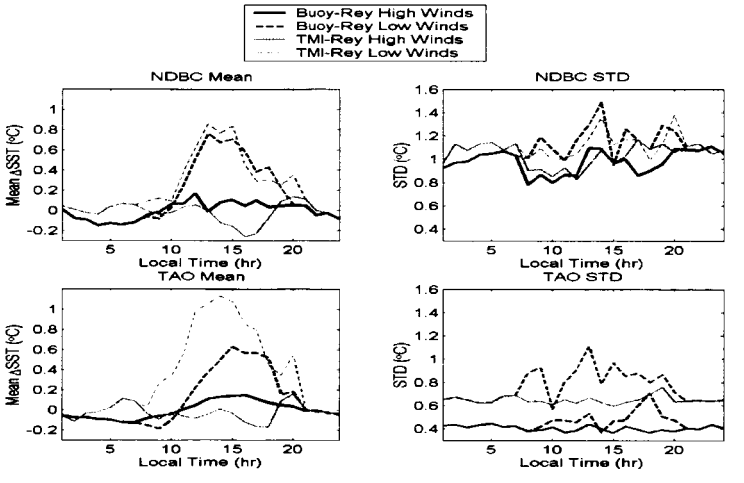

Figure 13. TMI and Buoy Diurnal Cycle: Mean SST difference and standard deviation (STD). Reynolds OI SST are subtracted from both the buoy SST and TMI SST to provide an unbiased estimate of diurnal magnitudes. For both SSTs, two cases are shown: solid line is for wind speeds between 6 m/s and 10 m/s, dashed line is for wind speeds less than 3 m/s. For both buoy datasets, NDBC and TAO, the mean difference and standard deviation is larger during the daytime for low wind speeds.

Mean SST differences are shown in the left-hand plots. The high-wind and low-wind cases show two distinctly different relationships between TMI minus OI ($\Delta SST_{subskin}$) and buoy minus OI (ΔSST_{bulk}). At high winds, the mean difference is very small, as any solar heating of the ocean surface is rapidly mixed into the bulk. At lower wind speeds, the mixing is suppressed, and a clear peak in near-surface SST can be seen. We expect that the solar heating of the surface will slowly diffuse to the deeper layers resulting in a smaller, delayed peak for the buoy data (at 1m) relative to the TMI (subskin) data. This effect can be seen in Figure 13, especially for the low-wind TAO measurements; the diurnal maximum of $\Delta SST_{subskin}$ is significantly larger than the maximum of ΔSST_{bulk} and it peaks one hour earlier. The right-hand plots show the standard deviations for each array of ΔSST. Both residual standard deviations increase during daytime for low wind conditions.

Figure 14 reveals the dependence of ΔSST on wind speed and local time. Each line represents a two-hour average, with daytime retrievals in red and nighttime retrievals in blue. During the daytime, ΔSST is largest at low wind speeds, decreasing with increased wind speed until 6 m/s, above which the mean residual for both comparisons remains constant. ΔSST_{bulk} is 0.95°C at 3PM while $\Delta SST_{subskin}$ is 1.65°C at 2 PM. Both plots also show a small amount of cooling during the nighttime at wind speeds less than 1 m/s. Interestingly, above 6 m/s, the $\Delta SST_{subskin}$ daytime constant value is less than the $\Delta SST_{subskin}$ nighttime constant, while the reverse is true for the ΔSST_{bulk} daytime/nighttime constant values.

These results have specific significance for the regression-based algorithms used to retrieve SSTs from the AVHRR sensor onboard NOAA satellites, especially for the afternoon polar orbiters, which drift from initial equatorial crossover times of 1:30 PM to 5:30 PM over their lifespan. Validation of both IR and MW satellite SSTs must take the relationship between *in situ* retrievals at 1m depth and the surface of the ocean into consideration.

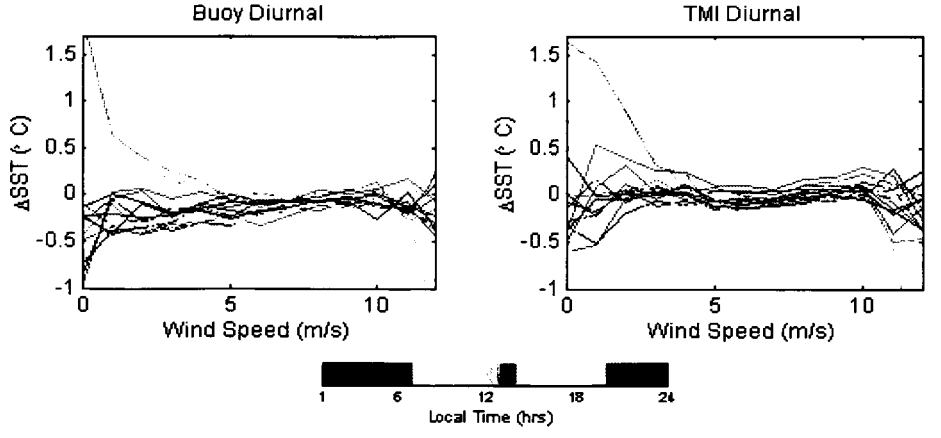

Figure 14. The dependence of the SST anomaly ΔSST on wind speed and local time of day. Local time is indicated by the color of the line. TMI has a larger ΔSST than the buoys. TMI and Buoy daytime ΔSST increases below 6 m/s. Daytime TMI values above 6 m/s are lower than nighttime values, while buoy daytime values above 6 m/s are higher than nighttime values. TMI nighttime values are fairly constant, decreasing at wind speeds less than 2 m/s.

5.2 Diurnal Variability: IR and MW satellite SSTs

In this study, Pathfinder (PF) SSTs from AVHRR and TMI SSTs are analyzed for diurnal warm layer effects by differencing them with the Reynolds OI SSTs. The diurnal warming measured by the satellite is used to construct a simple statistical model of diurnal warming. Model skill is examined through comparison of global patterns in the day minus night PF SST differences.

One significant difference between the TMI and PF datasets is that the diurnal cycle is only partially resolved by the PF dataset. At launch, NOAA satellite ascending equatorial crossover times is 1:40 PM, drifting to later equatorial crossover time as they age, therefore allowing limited temporal resolution of the diurnal cycle. The TMI orbit precesses through the diurnal cycle every 23 days. While this is extremely useful for complete resolution of the diurnal cycle, global mapping of the diurnal peak for comparison with AVHRR is more difficult, since at any given location and local time, it has 1/23 of the data. For this reason, we will restrict the global images of diurnal warming to AVHRR, but present globally averaged diurnal amplitudes from both datasets.

PF SSTs were collocated with daily average SSM/I wind speeds, daily-interpolated weekly OI SST fields, and daily average insolation. Over the open ocean, wind speed has virtually no diurnal cycle and the daily average wind should suffice for our analysis. Since the first SSM/I was launched in late 1987, we began collocation January 1, 1988 and continued through the end of the PF SSTs in August of 2001. The PF SSTs for 1991 are not available at this time due to difficulty correcting for large biases resulting from the Mt. Pinatubo eruption. TMI retrievals, extending from 1998-2001, have simultaneous wind speed and SST retrievals requiring no ancillary wind dataset, but need collocated interpolated weekly OI SST fields and daily average insolation values.

For the PF and TMI data, the collocated wind speed and insolation were used to construct a matrix of satellite SST minus OI SST (ΔSST) as a function of local time, wind speed, and insolation. At high wind speeds, the ocean is sufficiently well mixed such that skin (PF), sub-skin (TMI), and bulk (OI) retrievals should be closely coupled. To better compare diurnal amplitudes, at each local time we remove the overall bias at wind speeds for which the ΔSST became a constant. For TMI, the mean SST between 5.1 and 8.1 m/s was calculated for each local time and subtracted from the data. PF shows diurnal warming at wind speeds up to 10 m/s, so the mean SST between 12.1 and 15.1 m/s was subtracted.

The final 'correction' to the data, removes the nighttime cool skin effect, due to radiative cooling of the ocean surface. As wind speeds increase the thickness of the skin layer diminishes, changing the relationship between the skin PF measurement and the sub-skin TMI retrieval. By removing the cool skin at night, we can then examine diurnal warming, rather than diurnal warming in addition to the cool skin effect. For this reason, the 2 AM average difference as a function of wind speed was calculated and subtracted from the data. A second reason for this correction is unique to TMI. Although the magnitude of cooling seen at low wind speeds was comparable to *in situ* measurement (Donlon, 2002), it should not be trusted. Wind speed is an error that must be accounted for in the microwave SST retrieval algorithm, this is accomplished by tuning the TMI SST dependence on wind speed using the OI SST. The average difference, TMI minus

OI SST is designed to have a zero bias for all values of wind speed. At low winds, where there is diurnal warming of the daytime retrievals, all the retrievals will be cooled slightly to force a zero bias when averaged through the day. For this reason, we felt that it was better to simply examine diurnal warming magnitudes alone by subtracting out the 2 AM measurements of error and cool skin effect.

5.3 Development of an empirical model for TMI

We developed an empirical model of the diurnal warming using least-squares regression. The corrections mentioned above do not remove all errors in the data; therefore, we felt that a model that is consistent with our understanding of the physics of the problem could better describe the diurnal warming effect. For example, at low values of insolation, the PF day minus OI is negative. This is likely not due to diurnal warming but instead reflects the negative bias in daytime PF observations at high latitudes probably due to cloud contamination. In this case, using the actual data to calculate diurnal warming would be in error and a model that does not allow negative values would be better. When solar heating is very weak, there is no diurnal cycle and the model is set to zero. At higher insolation values, the daily average insolation is modulated by a diurnal function and by an exponential wind forcing.

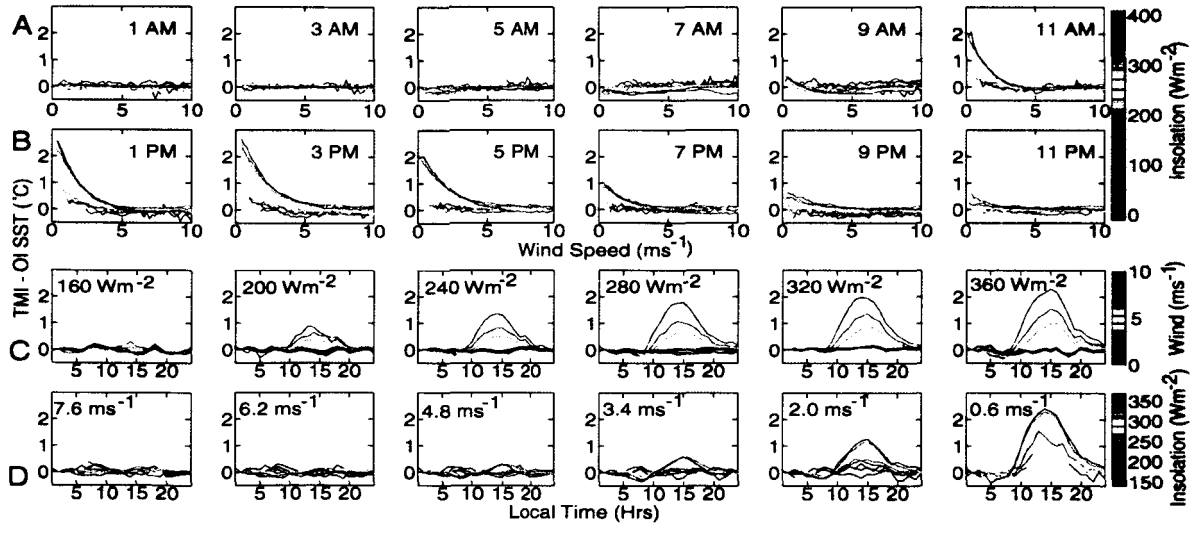

Figure 15. Diurnal warming from TMI. Rows A and B show ΔSST_{TMI} as a function of wind speed through the diurnal cycle. Daily average insolation is indicated by the color of the lines. Row C shows ΔSST_{TMI} through the diurnal cycle at several insolation values, with different wind speeds indicated by line color. Similarly, row D shows ΔSST_{TMI} through the diurnal cycle at several wind speeds, with insolation indicated by line color. To remove variability in the difference not due to diurnal warming and thereby highlight the diurnal amplitude, the average value for winds above 8.0 ms-1 and the cool skin effect was subtracted. The largest diurnal warming, 2.8°C, is at high insolation, low wind speed values at 3 PM.

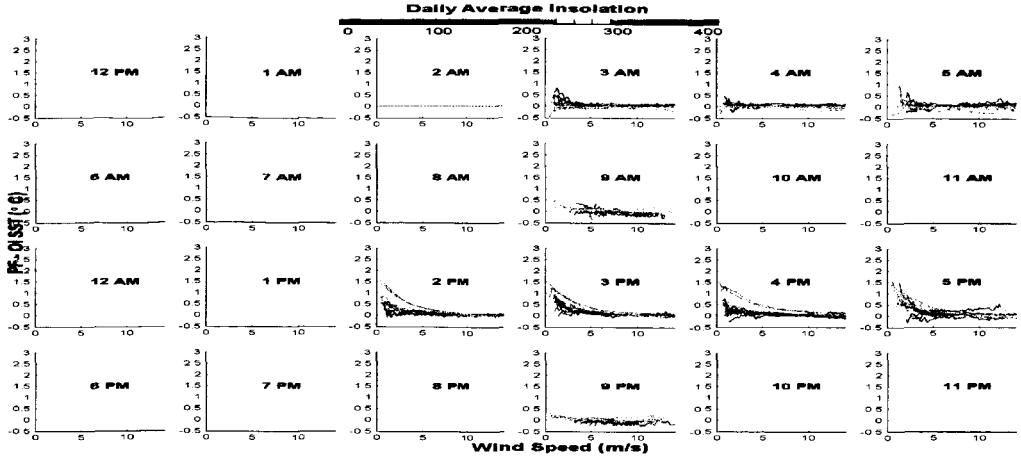

Figure 16. Diurnal Warming from PF. An average SST value for winds from 12.1 – 15.1 m/s is subtracted, for the same reason as in Fig. 15. The peak amplitude is 1.8°C at wind speeds of 0.6 m/s. Warming persists up to wind speeds of 10 m/s. Five hours of diurnal warming are resolved in the early morning and afternoon. There is additional information at 9 AM from November and December, 1994 when NOAA-11 failed and the algorithm reverted to NOAA-9 which had drifted far from its initial overpass time. The amplitude is largest at 2 PM, and then it diminishes through the afternoon.

The influence of wind speed and average daily insolation on diurnal warming is shown in Figure 15 (TMI) and Figure 16 (PF). At hourly intervals, the satellite minus OI SSTs are plotted as a function of wind speed for several daily average insolation values (indicated by the color of the line). In Figure 15, the complete diurnal cycle is resolved by TMI. Since the NOAA platforms are in a polar orbit, only parts of the diurnal cycle are resolved in Figure 16. Figure 15 shows that from 12PM to 6AM there are very few changes in the ΔSST difference. The PF temperature difference is constant relative to the OI SST at all wind speeds from 2 AM to 5AM.

At 7 AM, solar heating of the upper ocean begins, warming it as is shown in Figure 15. The data with strong insolation are warmed first, but even retrievals with weak solar heating show some warming from 11AM onwards. The amplitude of warming increases with time, reaching a peak at 2 PM of 2.8°C (Figure 15), and 1.8°C (Figure 16). The oceanic thermal inertia is large enough that vestiges of daytime heating are still present through midnight in Figure 15. For both the PF and TMI measurements of diurnal warming, the amplitude diminishes exponentially in wind speed and linearly in insolation to a constant value above approximately 10 m/s and 5 m/s, respectively, and is a function of local time.

A comparison of the diurnal amplitudes is shown in Figure 17. Here, the diurnal cycle is shown for both TMI and PF comparisons, at 1.35 m/s and 330 W/m^2 daily average insolation. The shape of diurnal warming is not sinusoidal, but would perhaps be best modeled by a skewed bell curve. At 2 PM, the peak time for diurnal warming, TMI and PF match very closely. The warming is present until 1 AM.

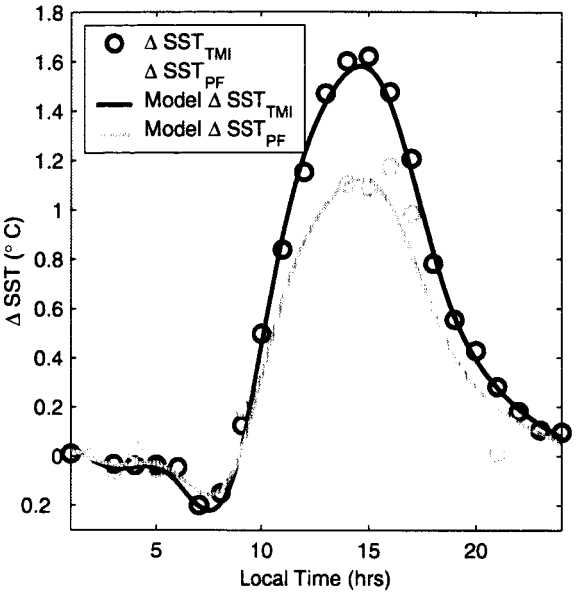

Figure 17. The diurnal cycle at 1.2 ms-1 wind speed and 320 Wm-2 insolation. Plotted on the figure are ΔSSTTMI (black circles), modeled ΔSSTTMI (black line), ΔSSTPF (gray circles), and modeled ΔSSTPF (gray line) as a function of local time. The cool skin effect was removed from the data, so night ΔSST is zero at 2 AM.

When solar heating is weak, below 132 Wm-2 (24 Wm-2), there is no discernable diurnal cycle in the TMI (PF) data and the model is set to zero. Figure 17 shows a comparison of the TMI and PF SST data and modeled diurnal cycle at 1.2 m/s and 320 Wm^{-2} insolation. Since the shape of the diurnal cycle for the PF and TMI SST retrievals should be identical, a complete model can be created for the PF, using the PF amplitude modeled on the shape of the TMI diurnal cycle. In Figure 17, the PF data fits reasonably well to the modeled shape. The early morning minimum seen in Figure 15 is clearly revealed here. Although all diurnal warming has vanished by midnight, at low wind speeds there is a larger cool skin effect causing an early morning minimum. Figure 17 also clearly shows that the amplitude of warming is larger in the TMI SSTs than in PF SSTs. We expect that the PF amplitude to be slightly under-estimated, since without a time of observation for each PF SST retrieval we end up averaging over a range of local times due to swath width and orbital inclination. Figure 17 also includes the amplitudes modeled by (1a) and (1b). The model compares very well with the shape of the data; requiring only wind speed and daily average solar insolation as inputs.

Global maps of diurnal warming can be calculated from the model and subtracted from the satellite SST to remove diurnal effects. Some examples of the correction to the PF data are shown in Figure 18 and Figure 19. A month of averaged PF day minus night SSTs, SSM/I wind speed, modeled diurnal warming, and corrected PF day minus diurnal minus night SSTs are shown in Figure 18 from top to bottom respectively. Regional biasing is present in the top panel, particularly evident in the western Tropical Pacific, and is corrected in the bottom panel. Another demonstration of this bias reduction is shown in Figure 18, which shows the annually averaged uncorrected PF day minus night (left column) and corrected fields (right column).

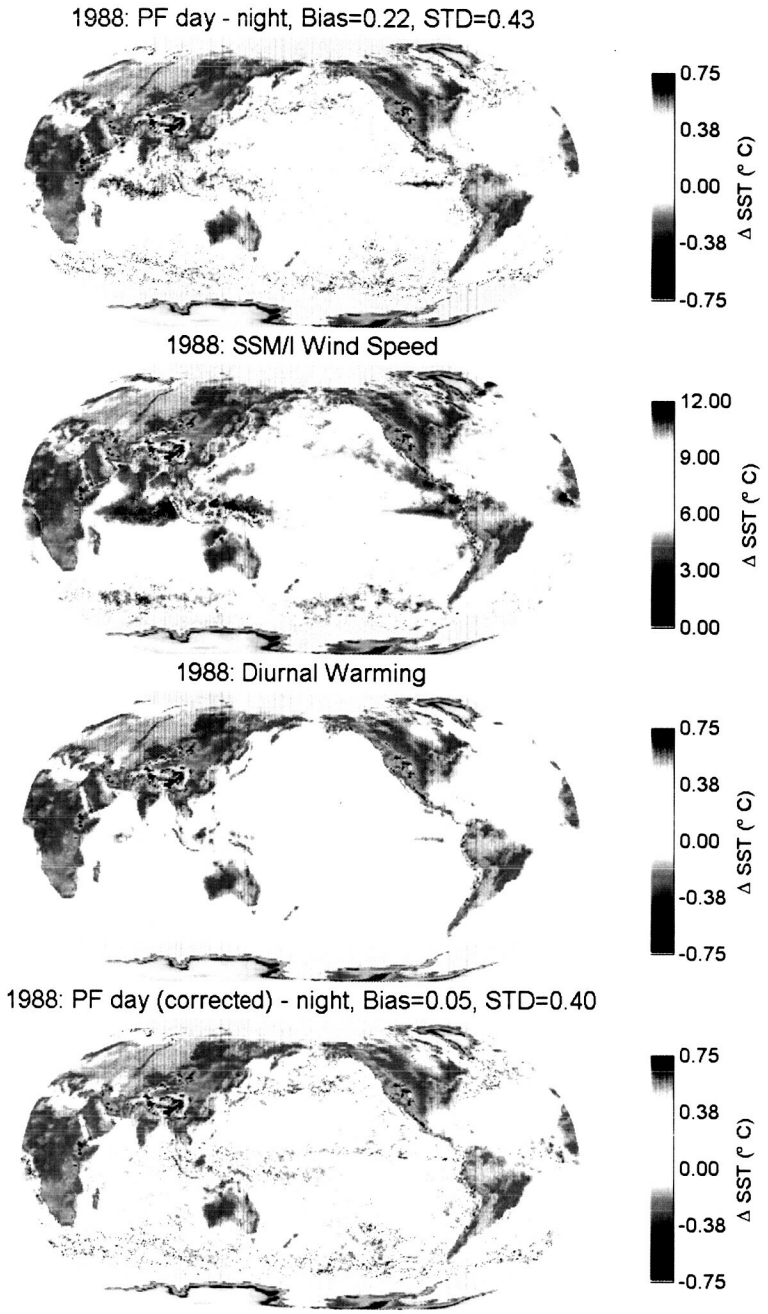

Figure 18. Correction for diurnal effects in SSTs. From top to bottom, Pathfinder AVHRR day minus night SST, SSM/I average wind speed, diurnal warming, corrected PF day minus night SSTs.

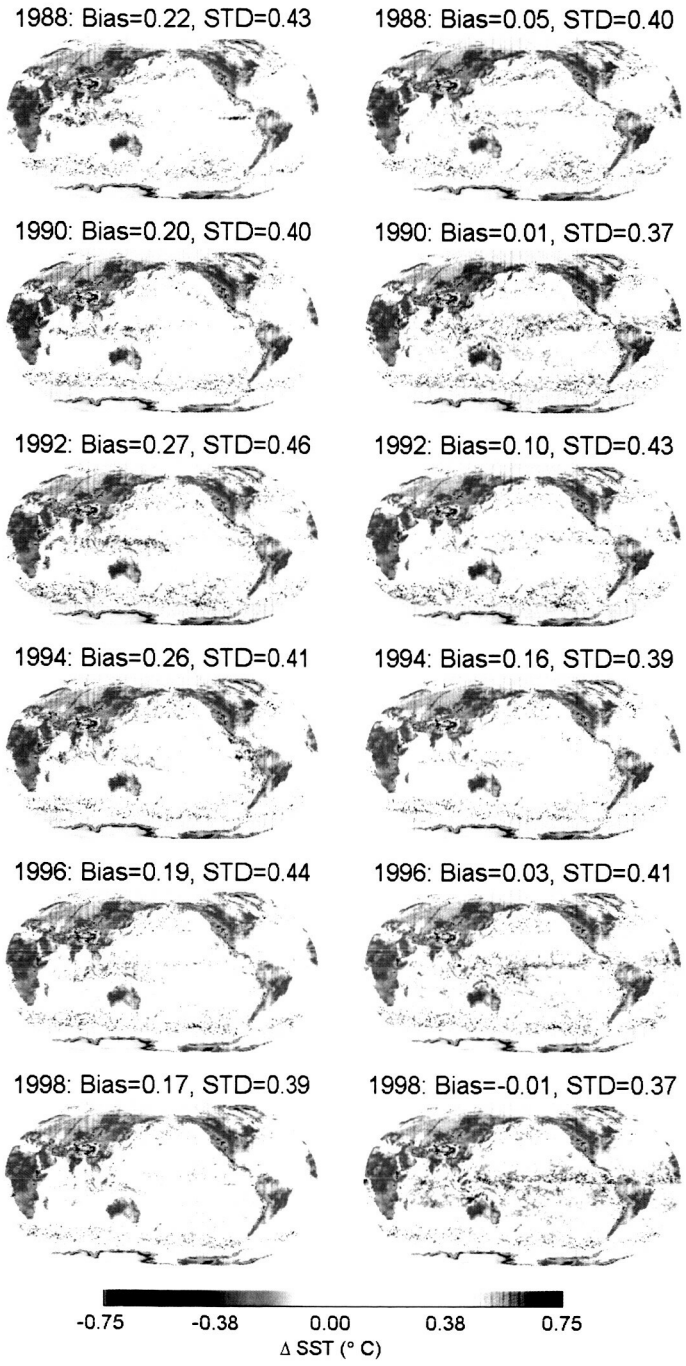

Figure 19. PF day minus night SSTs for 1988 through 1994. The left column shows uncorrected PF day minus night difference while the right column shows the PF day minus night, corrected for diurnal warming using Eq. 1. In all cases the bias and STD are reduced.

5.4 Comparisons to diurnal warming measured by AVHRR

In conclusion, two independent satellite datasets show extremely good agreement with modeled skin-bulk differences. The magnitude of diurnal amplitudes witnessed by the satellite data and verified by the model data testify to the importance of understanding diurnal warming. TMI measures through the complete diurnal cycle and verifies several features seen in the model, such as diurnal warming lasting until 11 PM. The amplitudes shown by the model are larger than the satellite values. Some features of the satellite data are recognized as algorithm / regional biases through comparison with the model. The 'corrected' satellite data are included in calculation of a statistical skin-bulk model of diurnal warming that utilizes an ancillary wind field. The statistical model is then applied to daytime PF SST, removing the majority of regional biases and decreasing the daytime bias and STD. The statistical model developed is simple to apply and could be applied to real time multi-sensor blended SSTs.

5.5 Comparison to diurnal warming measured by moored buoys

Continued development and fine-tuning of the model presented in the previous quarterly progress reports was completed. The results, accepted for publication by *Geophysical Research Letters,* have been extended to include 13 years of NDBC buoy data. RSS has a large buoy dataset, which has been carefully quality-controlled. The dataset includes all moored buoy arrays, but we used only NDBC in this study as the latitudinal variability in that set of buoys is larger than the one contained in the tropical PIRATA and TAO arrays.

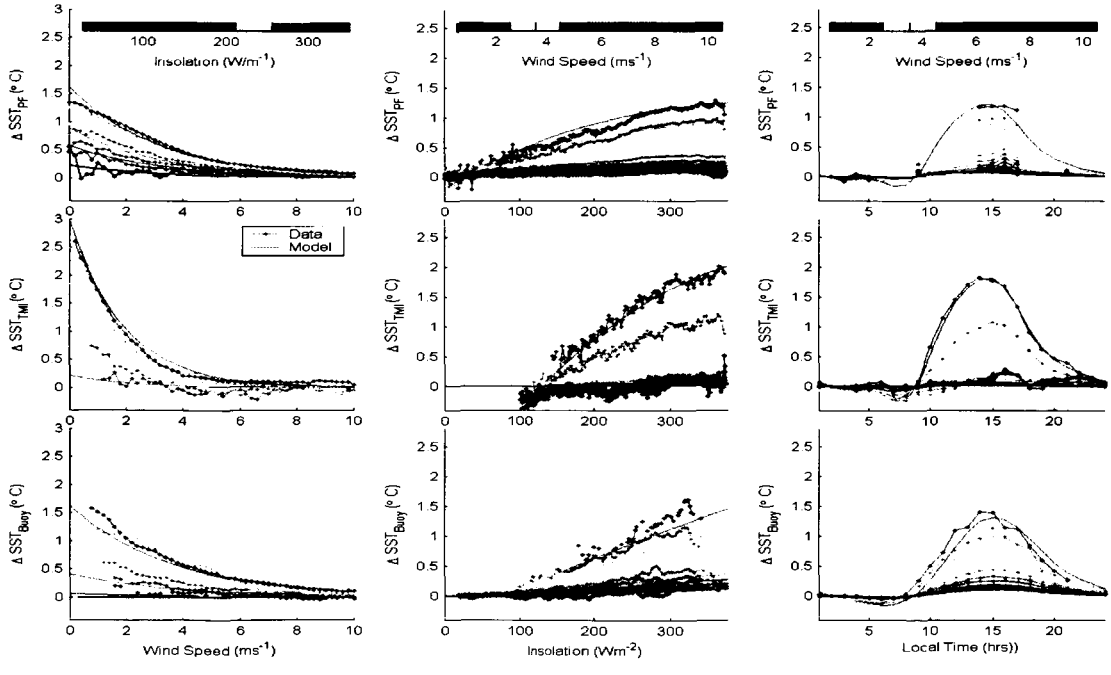

Figure 20. From top to bottom: PF SST, TMI SST, and Buoy SST diurnal warming. The right column shows the dependence on wind speed, the center column shows the dependence on insolation and the left column shows the shape of the diurnal cycle through the day.

The buoy data were processed using the same methodology described above. The diurnal amplitudes for buoy SSTs are smaller (about 1°C) and the peak is about 30 minutes later than TMI's diurnal peak. As discussed in the last progress report, we derived a model for the diurnal excursion, ΔSST (°C), where Q is insolation (Wm^{-2}), t is time (hr) and u is wind speed (m/s), as follows:

$$\Delta SST_{tmi}(t,Q,u) = f_1(t)[(Q-Q_o^t) - 9.632\times10^{-4}(Q-Q_o^t)^2]e^{-0.53u}\Big\} \text{for } Q \geq Q_o^t \quad (1a)$$

$$\Delta SST_{pf}(t,Q,u) = 0.344 f_1(t)[(Q-Q_o^p) - 1.444\times10^{-3}(Q-Q_o^p)^2]e^{-0.29u}\Big\} \text{for } Q \geq Q_o^p \quad (1b)$$

$$\Delta SST_{buoy}(t,Q,u) = f_2(t)[(Q-Q_o^b) - 4.928\times10^{-4}(Q-Q_o^b)^2]e^{-0.28u}\Big\} \text{for } Q \geq Q_o^b \quad (1c)$$

$$f_1(t) = [6.814 - 6.837\cos(\omega_1 t) - 8.427\sin(\omega_1 t) + 1.447\cos(2\omega_1 t) + 4.274\sin(2\omega_1 t) - 0.407\cos(3\omega_1 t) - 0.851\sin(3\omega_1 t)$$
$$+0.457\cos(4\omega_1 t) - 0.555\sin(4\omega_1 t) - 0.101\cos(5\omega_1 t) + 0.375\sin(5\omega_1 t)]\times 0.001$$

$$f_2(t) = [3.611 - 2.051\cos(\omega_2 t) - 3.707\sin(\omega_2 t) + 0.102\cos(2\omega_2 t) + 1.217\sin(2\omega_2 t) + 0.074\cos(3\omega_2 t) - 0.144\sin(3\omega_2 t)$$
$$+0.014\cos(4\omega_2 t) - 0.016\sin(4\omega_2 t) + 0.027\cos(5\omega_2 t) - 0.025\sin(5\omega_2 t)]\times 0.001$$

where $\omega_1 = 0.2668 hr^{-1}; \omega_2 = 0.2652 hr^{-1}; Q_o^t = 132 Wm^{-2}; Q_o^p = 24 Wm^{-2}; Q_o^b = 88 Wm^{-2};$

A comparison of the data and the derived model is shown in Figure 20. The buoy dataset was very interesting as the 1-m temperature is often assumed to be basically free of diurnal variability. Equation 1c shows that the wind speed dependence derived for the buoy dataset is very similar to the wind speed dependence seen in the PF skin SSTs. The amplitude of the diurnal signal is larger for the buoy 1-m SSTs than for the PF SSTs, while the diurnal amplitude is zero at wind speeds above 6 m/s for TMI, but is still positive until 10 m/s for the buoy SSTs. These results suggest that individual satellite algorithms and biases can affect their measurement of diurnal warming. It is likely that the diurnal amplitude in the PF SSTs was artificially diminished through one step in the cloud-clearing algorithm where the SST is compared to Reynolds OI SST. If the PF SST is different by more than 2 degrees, it is flagged as cloudy. This step mistakenly removed the diurnal warming too. On the other hand, the TMI shows no diurnal warming above 6 m/s wind speed, but this is likely incorrect since both the PF and buoy SST s show warming until 10 m/s. The TMI algorithm has been tuned to remove all cross-talk with wind and it is likely that it is over-correcting and mistakenly removing diurnal warming between 6 and 10 m/s.

These results suggest that each sensor and algorithm combination should likely have a unique empirical diurnal warming model, to accurately reflect the warming contained within the individual dataset. But, each model will have elements of truth that can be combined to create an empirical model that will accurately reflect the actual diurnal warming present.

6 VIRS/TMI SST inter-comparison

The availability of both infrared (VIRS) and microwave (TMI) sensors onboard the Tropical Rainfall Measurement Mission (TRMM) provided an opportunity to perform our detailed SST inter-comparison from two distinct but perfectly co-located sensors. Infrared (IR) retrievals provide good spatial resolution but they are affected by clouds and atmospheric water vapor, and are therefore limited to clear sky conditions.

Microwave (MW) observations provide supplemental SST information in cloudy areas, but they are subject to other limitations like poor spatial resolution and possible wind biases.

We analyzed one year of co-located VIRS and TMI SSTs, together with other co-located ancillary datasets including surface winds and water vapor from TMI. In particular, we focused on the effects on SST retrievals of: high winds, land contamination, atmospheric water vapor, undetected clouds, choice of IR SST algorithm, satellite maneuvers and calibration errors. In addition, both the datasets were used to investigate the amplitude of the diurnal variation of skin SST.

Daily maps of VIRS SSTs are produced and supplied by the Earth Observation Research Center of the National Space Development Agency (NASDA) of Japan. In order to co-locate the VIRS observations with TMI, have the flexibility to test several IR algorithms and then perform the analyses described here, we processed VIRS brightness temperatures from the orbital files and created our own versions of VIRS SSTs. The VIRS SSTs we produced are not distributed and they were created exclusively for research purposes.

The creation of a VIRS SST dataset involved three major steps: the development of an efficient cloud detection algorithm able to select clear-sky observations, the use of an additional SST dataset in order to calculate regression coefficients for the different forms of the multi-channel SST algorithm, and finally the calculation of SSTs from VIRS brightness temperatures.

6.1 Cloud detection algorithm

For an efficient detection of cloud contaminated retrievals using VIRS visible and IR channels, we relied on the well-tested cloud mask developed for the AVHRR (May et al., 1998). The cloud algorithm developed for AVHRR data can be easily modified to detect clouds with VIRS during nighttime, as only IR channels are involved. During the day, visible and near-IR channels are very helpful in cloud detection, since the cloud reflectivity is much higher than the ocean background. Generally, a simple threshold on reflectivity can discriminate cloud-contaminated observations. However, for particular sun-satellite viewing angles, such as at high solar zenith angles or when the satellite is looking in the direction of specular reflection of solar radiation (sun glint), the ocean reflectivity is high even for clear sky and the simple reflectivity threshold method cannot be applied. Since VIRS is on an inclined orbit, the cloud mask needs to address a wide variety of sun-satellite configurations, unlike the AVHRR that is onboard polar orbiters.

In order to maximize the number of successful VIRS retrievals during daytime, we developed a method to adjust the reflectivity to normal conditions in these particular cases, allowing us to use the threshold method to discriminate clouds. For this purpose, we used one year of selected clear-sky VIRS data, determined with restrictive thresholds and tests, to develop statistical information about reflectivity for different viewing geometries. For each channel, a polynomial fit R_{FIT} was calculated from the observed reflectivities R_{OBS} separately as a function of the solar zenith angle (SZA), the scan angle (SCAN) and the sun glint angle (SG) , and compared to unaffected clear-sky water

reflectivity R_{NORMAL} . We calculated an empirical adjustment function $ADJ_{SZA,SG,SCAN}$ for each viewing effect expressed as the ratio between R_{NORMAL} and $R_{FIT(SZA,SG,SCAN)}$. The adjusted reflectivity at each observed pixel i and each channel is:

$$R_{ADJ}(i) = R_{OBS}(i) \cdot ADJ_{SZA}(i) \cdot ADJ_{SG}(i) \cdot ADJ_{SCAN}(i)$$

As an example, Figure 21 shows the VIRS Ch. 1 reflectivity before and after the adjustment.

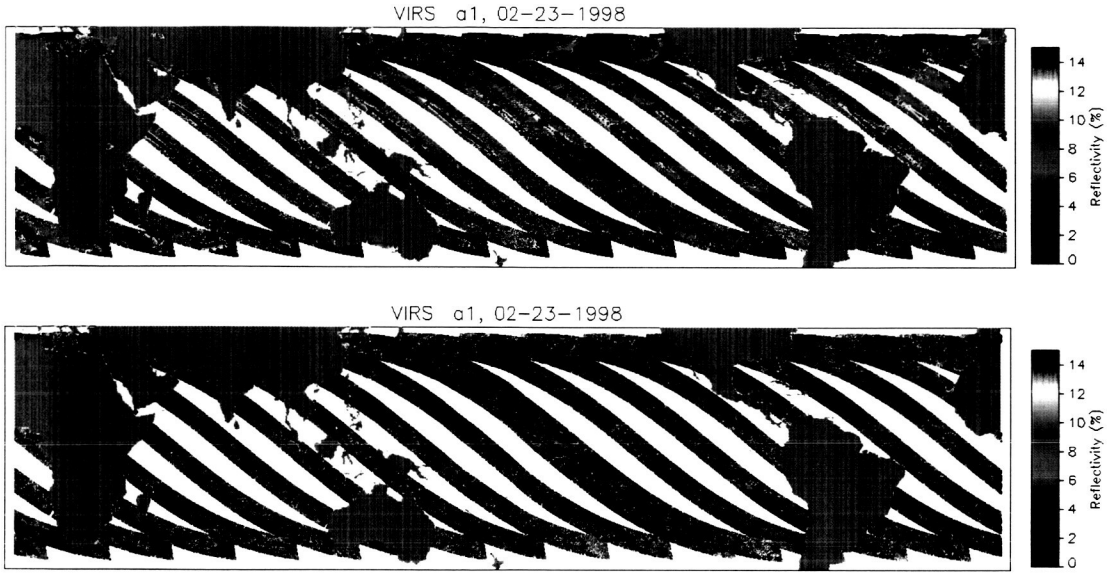

Fig. 21: VIRS clear-sky Ch. 1 reflectivity map for February 23, 1998, as observed (top panel). The figure clearly shows sunglint regions in the left side of the scans, and high solar zenith angle effects at the higher latitudes for this particular day. After the reflectivity adjustment described in the text, cloud-contaminated pixels are clearly identified in the areas depicted in red (bottom panel).

An efficient cloud detection test in daytime is to flag as cloud-contaminated all pixels for which the empirically adjusted reflectivity is greater than a threshold value. We chose the thresholds to be 8% and 6% for Ch. 1 and 2, respectively. In addition to daytime tests on reflectivity, the cloud detection algorithm we applied to VIRS data is a suite of tests on spatial coherence, and on cirrus and low stratus clouds detection by comparing the brightness temperatures detected by pairs of IR channels, very similar to the AVHRR tests described in May et al. (1998). We applied the tests on 2x2 pixels, resulting in a 4 Km spatial resolution.

6.2 VIRS SST algorithms

After applying the cloud mask, VIRS SSTs can be determined from the observed brightness temperatures using an IR algorithm. Here we focused on the multi-channel algorithms (McMillin and Crosby, 1984; McClain et al., 1985), currently adopted for many operational SST products. These algorithms are based on the assumption that the brightness temperature observed by the satellite can be represented in terms of the surface temperature and an atmospheric correction term proportional to the difference between two channels, which represents an estimate of the atmospheric absorption mostly due to water vapor. Several forms of the multi-channel algorithms have been developed in recent years and are extensively described in Barton et al. (1995), Walton (1988), Emery et al. (1994), and Walton et al. (1998). One objective of our IR/MW inter-comparison is to assess the ability of some of these algorithms to correct for atmospheric attenuation and satellite viewing configurations. We investigated SSTs obtained from the following algorithms: the non-linear sea surface temperature algorithm (*NLSST*), conventionally adopted for AVHRR radiances; the linear multi-channel SST algorithm (*MCSST*) adopted by NASDA in their processing of VIRS SSTs. In addition to these conventional algorithms, we also experimented two alternative algorithms ($WVSST_{1,2}$) that include co-located MW water vapor, rather than the brightness temperature channel difference.

$$NLSST = a + bT_4 + c(T_4 - T_5)SST_{fg} + d(T_4 - T_5)(\sec\vartheta - 1)$$

$$MCSST = a + bT_4 + c(T_4 - T_5) + d(T_4 - T_5)(\sec\vartheta - 1)$$

$$WVSST_1 = a + bT_4 + cT_5 + d \cdot W_v + e \cdot W_v(\sec\vartheta - 1)$$

$$WVSST_2 = a + bT_4 + cT_5 + d(T_4 - T_5)SST_{fg} + e \cdot W_v + f \cdot W_v(\sec\vartheta - 1).$$

Here, T_4, and T_5 are the brightness temperatures observed by channel 4 and 5 on VIRS, respectively; SST_{fg} is a first guess SST (in our case from TMI), ϑ is the satellite zenith angle; and W_v is the co-located water vapor from TMI. The four algorithms displayed here refer to daytime. Night algorithms are slightly different as they also include brightness temperatures T_3 from the near-IR channel 3. In addition to the listed algorithms, other variations of these algorithms were tested to evaluate the significance of the atmospheric correction terms in the algorithms. They will not be discussed in detail in this paper as their performance deteriorated the SST retrieval.

The coefficients *a*, *b*, *c*, *d*, *e*, *f* and *g* in the algorithms were estimated by regressing cloud-free VIRS brightness temperatures to one year of co-located TMI SSTs, separately for day and night and for each algorithm. TMI data in presence of wind speeds greater than 12 m/s were excluded from the regression in order to avoid biases in microwave SST retrievals due to high winds. A set of orbital VIRS SSTs for the year 1998 was created for each tested algorithm, at a spatial resolution of approximately 4 Km. The orbital data were then gridded on daily 0.125x0.125 deg tropical maps from January 1 until December 31, 1998. More VIRS SSTs are currently under processing for data until 2002.

Daily maps of VIRS SSTs for the entire 1998 were compared to daily co-located TMI SSTs, OI SSTs and the VIRS SST daily maps provided by NASDA, showing general

agreement. The adjustment applied on reflectivities resulted in successful retrievals even in sun glint regions, unlike the maps provided by NASDA.

6.3 VIRS/TMI SST inter-comparison

When compared to TMI observations for the entire 1998, VIRS SSTs did not show any significant bias, as expected. The average standard deviation of (VIRS-TMI) daily SST maps was found to be 0.7 C, for both day and night retrievals with the NLSST algorithm. Slightly higher values for the standard deviation, up to 0.8 C, were found for the other three algorithms especially those not constrained by the first guess TMI SST. Comparison of VIRS SSTs with diurnally interpolated Reynolds OI SSTs also did not show any bias for 1998 data. An average standard deviation of 0.7 C was found when comparing daily VIRS maps versus diurnally interpolated Reynolds SSTs. A similar value was found for the standard deviation of daily TMI SST versus daily-interpolated Reynolds OI SSTs. Finally, to complete the validation of our VIRS SSTs, we compared them to daily maps of VIRS SST provided by NASDA. In this case the standard deviation was 0.45 C, without bias. Despite the average bias for VIRS data compared to TMI or Reynolds SSTs is zero, temporal variations in a 0.5 C range do occur, particularly in correspondence of yaw changes in the TRMM satellite. The time series of VIRS-TMI SSTs also shows a variation with a cycle of approximately 40 to 50 days, which might be due to a "diurnal cycle" of the TMI antenna, which observes the earth at a different local time for each day, precessing every 46 days.

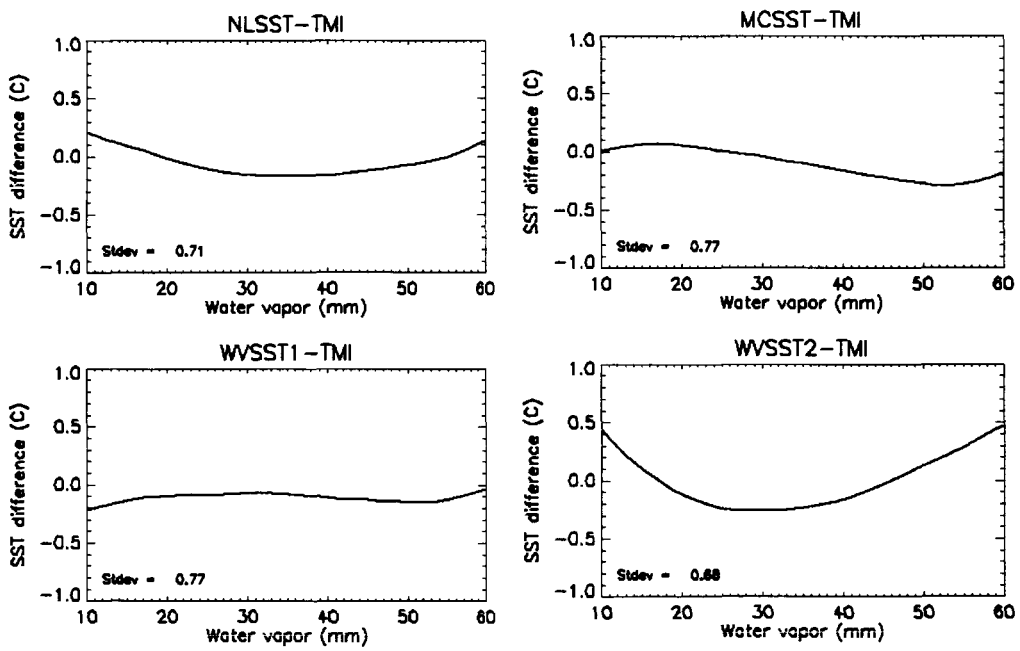

Figure 22: VIRS-TMI SSTs as a function of the atmospheric water vapor column. The SST differences are averaged over one year (1998), for the four tested algorithms: NLSST, MCSST, WVSST1, and WVSST2.

To correct for atmospheric water vapor effects, the most of the IR SST algorithms rely on the differential absorption by pair of thermal channels *(i,j)* , represented by the term $(T_i - T_j)$. However, some of the assumptions these algorithms are based on might not be valid under all atmospheric conditions. For this reason, we analyzed the residual dependence of each VIRS algorithm's SSTs on atmospheric water vapor. Without the correction for atmospheric water vapor, the VIRS-TMI difference would have a negative bias at high water vapor. In Figure 22 we see that both *NLSST* and $WVSST_2$ have a residual warm bias (~0.3-0.5C) at high and low water vapor, possibly the effect of an over-correction by the non linear term which includes SST_{fg}. The simpler *MCSSTs* have a minor residual dependence on water vapor with a very small cold bias for water vapor > 50 mm. When water vapor is explicitly considered in the algorithm $WVSST_1$, the VIRS SSTs do not show significant residual water vapor effects.

The VIRS instrument scans a +/- 45 deg angle in 261 pixels. The increased pathlength at high satellite zenith angles ϑ results in greater attenuation of IR radiation by water vapor and other atmospheric constituents. The brightness temperatures observed at the edge of the scan are colder than those observed at the center of the scan, and the difference depends on the satellite angle ϑ, the sensor's channel wavelength and the water vapor column in the observed regions. For VIRS Ch. 5, the brightness temperature T_5 at the edge of the scan is about 2K colder than the one at the center of the scan for high water vapor conditions (W_V > 50 mm). For this reason, all the SSTs algorithms include the term $F_\vartheta = \sec(\vartheta) - 1$ to correct for increased pathlength at high satellite viewing angles. Despite the corrective term, we found some residual dependence on scan angle ϑ affecting the VIRS SST retrievals, in particular with *NLSST* and $WVSST_2$.

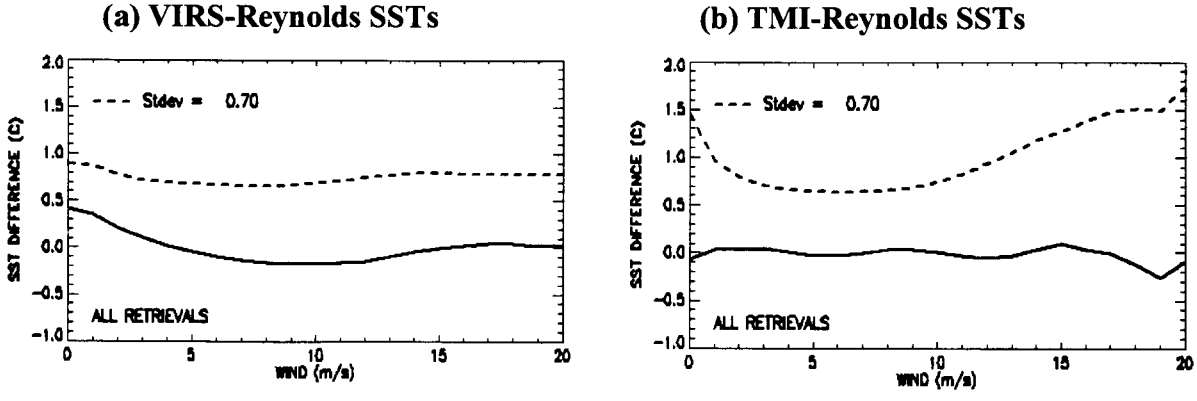

Figure 23: VIRS(NLSST)-Reynolds daily interpolated SSTs (left panel) and TMI-Reynolds (right) for 1998 data. The figures show the average difference (solid line) for all retrievals (day and night), and its standard deviation (dashed line) as a function of surface wind speed.

In order to study the effects of winds on MW and IR SST retrievals, we analyzed the difference between VIRS or TMI SSTs and the daily-interpolated Reynolds SSTs, as a function of surface wind speed. Except for low winds, VIRS SSTs (Figure 23a) do not

seem to be affected by wind speed, both in terms of bias and standard deviation. At low wind speeds, less than 5 m/s, the VIRS SSTs during the day are warmer than the Reynolds SSTs, because of the effects of the diurnal warming of the ocean skin layer. The differences between TMI and Reynolds SSTs are illustrated in Figure 23b, as a function of wind speed. Because of the MW algorithm implicitly accounts for ocean MW emissivity as a function of wind speed, on the average TMI SSTs do not show any bias due to wind effects. However, at high wind speeds we notice a significant increase in the standard deviation. Therefore, even if not biased, TMI SSTs at high wind speeds have a greater uncertainty. At low wind speeds, TMI SSTs show the effects of diurnal warming, similarly to VIRS SSTs.

In Figure 24 we show the difference between VIRS (NLSST algorithm) and Reynolds SSTs as a function of the local time of the day, for one year of data in all wind conditions, and for low winds only (less than 3 m/s). A significant diurnal variability is evident for the VIRS SSTs in low winds, as a result of the solar warming of the skin layer. The amplitude of the diurnal signal is on the average of the order of 1 C, with a peak value at about 2 PM, and slowly decaying even after the local midnight. The minimum temperatures are found in the early morning hours, at about 6 AM. The difference between TMI and Reynolds SSTs highlights a similar diurnal signal for TMI at low winds. One major difference between VIRS and TMI diurnal cycle is an apparent night cooling in the TMI SSTs, which could be a geophysical feature or an artifact of the processing operations on TMI data.

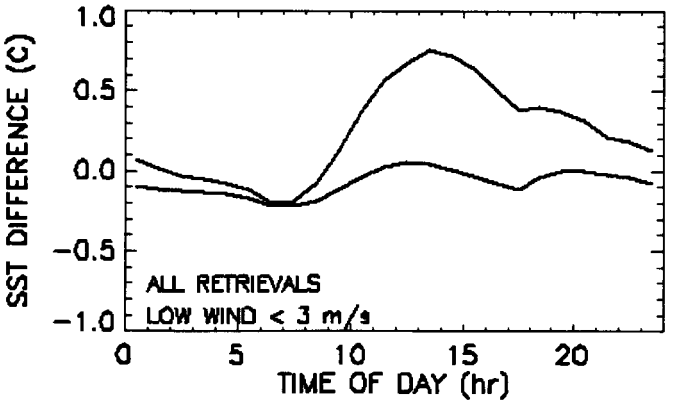

Fig. 24: VIRS(NLSST)-Reynolds daily interpolated SSTs as a function of the local time of the day. The differences are averaged over one year of data, for all retrievals (blue) and in low wind conditions only (red line).

Microwave observations in the proximity of land are affected by the warm emission of land entering the antenna near-in sidelobes. This warming of the microwave brightness temperatures is a source of errors in the TMI retrievals of coastal waters. Since infrared retrievals are not affected by land emission, the difference between TMI and VIRS SSTs is a good indicator of the bias of TMI SSTs due to land contamination. Figure 25 shows differences between TMI and VIRS (NLSST algorithm) SSTs for a sample region, Hawaii, averaged over one month (January 1998). The land contamination produces a systematic warm bias of TMI SSTs of the order of 1C in regions within 50-100 Km from land.

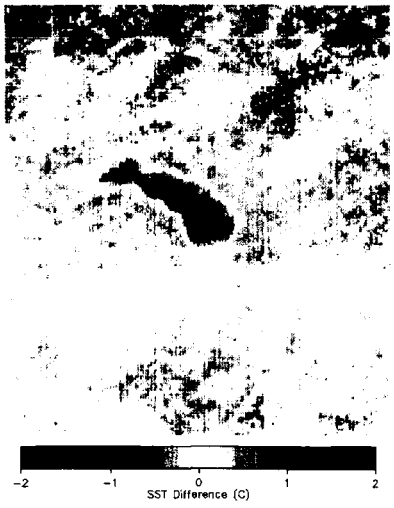

Fig. 25: Monthly average SST difference between TMI and VIRS(NLSST), for January 1998, for the coastal waters of Hawaii. Similar warm bias was found along all coastlines in the TMI data.

These results showed that both infrared and microwave observation of the ocean temperature can benefit from the inter-comparison. After the major reasons for differences between VIRS and TMI SSTs are excluded (high winds, diurnal signal, water vapor, viewing geometry, satellite maneuvers and calibration errors), the residual differences might be due to undetected clouds or aerosols in infrared retrievals. Currently, most of the cloud detection algorithms apply a constant threshold (or one dependent on brightness temperature) to channel differences $(T_i - T_j)$ to discriminate clear sky observations. In reality, these differences are highly dependent on the atmospheric conditions. As an example, in Figure 26 we show the probability distribution function of one year of observed channel T differences, as a function of atmospheric water vapor. In the future, the correlation range between brightness temperature differences and water vapor can be used as an additional physically based cloud test. Therefore, the IR/MW comparison can also lead to an improvement in the efficiency of the IR cloud mask.

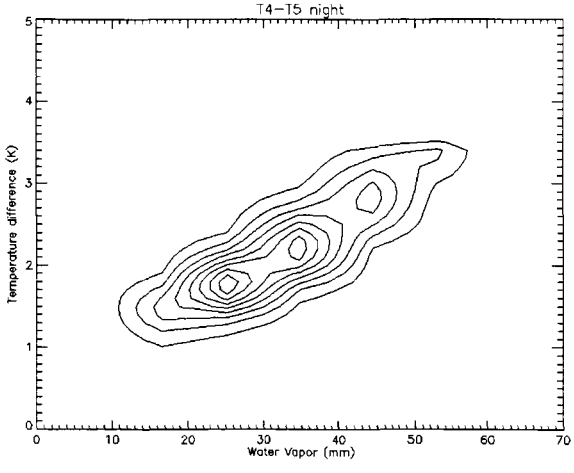

Fig. 26: Probability distribution function of brightness temperature channel difference versus water vapor for VIRS observations averaged over a 4x4 Km box for night retrievals of (T4-T5).

7 Research applications

7.1 Tropical Instability Waves

Early satellite observations of sea-surface temperature in the Pacific and Atlantic exposed the existence of westward-propagating waves a few degrees north of the equator with wavelengths, periods and phase speeds of about 1000 km, 21 days, and 0.5 m/s. Models and observations conclude that these waves are generated by instabilities of the equatorial currents. The waves are thus referred to as tropical instability waves (TIWs).

To study these phenomena, TMI SST measurements were composite averaged over 3-day periods. The TMI data clearly show the synoptic temporal evolution of TIWs, and allow examination of the development and evolution of the various features, such as cusps and tongues, on both sides of the equator.

The microwave measurements of SST reveal previously unreported features of TIWs: SST signatures of TIWs are evident on *both* sides of the equator in the Pacific with about 50% larger amplitude in the north; the northern band of short-period Pacific SST variability indicates that TIW signals extend from 100°W to the east; Pacific TIWs propagate farther west than the date-line, perhaps all the way to the western boundary, although this cannot be determined from SST. This work is best summarized in a paper, *Microwave SST Observations of Transequatorial Tropical Instability Waves* by Chelton, Wentz, Gentemann, Szoeke and Schlax.

Combining TMI SST measurements of the TIWs with coincident retrievals of wind speed and wind direction from QuikSCAT has yielded new insight into air-sea interactions. These cold ocean waves appear to be damping low-level atmospheric winds by cooling the atmosphere, which stabilizes the boundary layer, thereby inhibiting vertical transfer of momentum from a jet aloft. This work is best described in two papers: *Observations of Coupling Between Surface Wind Stress and Sea Surface Temperature in the Eastern Tropical Pacific*, by Chelton, Esbensen, Schlax, Thum, Freilich, Wentz, Gentemann, McPhaden, and Schopf, and *Two Satellites Observe Details of Ocean-Atmosphere Coupling*, by Charles Day.

7.2 Testing TMI SSTs in NCEP OI SSTs

We have continued the collaboration with Dick Reynolds at NOAA to include TMI SSTs in his weekly NCEP OI SSTs (also known as Reynolds SSTs). During the last quarter we began preparing a paper. This work continued into this quarter with some major changes to the paper. It has now been submitted to the Journal of Climate entitled: "Impact of TRMM SSTs on a Climate-Scale SST Analysis". During this quarter a comparison to Bob Weller's IMET buoy off the coast of Peru was added to the paper. The TMI SSTs used in the analysis were switched from weekly separate day and night datasets to weekly combined day and night data, and we tried to address a bias between the satellite and in situ data seen in the North Pacific.

For the OI analyses with bias correction, it is difficult to clearly demonstrate that there is a significant advantage in adding TMI. This conclusion was based on analysis inter-

comparisons and the use of the independent data. The use of the moored research buoy located off the coast of Peru was an important addition to the set of independent data. The comparisons with this buoy showed only a slight advantage in combing both AVHRR and TMI data in a bias corrected version of the OI. However, the advantage of TMI data was clearly shown in the OI analyses without bias correction. Because IR and microwave satellite algorithms are affected by different sources of error, biases tend to be reduced when both TMI and AVHRR data are used in the OI. The use of both TMI and AVHRR data improves the OI analysis without bias correction and does not negatively impact the OI analyses with bias correction. Because there are many areas of the ocean with limited in situ data and restricted AVHRR coverage due to cloud cover, the use of both TMI and AVHRR should improve the accuracy of the analysis in these regions. In addition, the use of more than one satellite product is helpful in diagnosing problems in these products.

In the first draft of the paper, we divided the TMI data into day and night categories. The division was defined by local time of the retrieval. Day is defined by times between 8 A.M. and 8 P.M., while night was the remainder. However, the analyzed results tended to be noisy at higher latitudes due to sparse sampling as discussed at the beginning of the next section. Thus, the TMI product used in our final version of the OI analyses was a combined product in which day and nighttime data were averaged together based on the total number of observations.

Finally, we looked more into the North Pacific region. The need for positive bias corrections in TMI and AVHRR north of 30°N in the Pacific could indicate an in situ data problem, because the TMI and AVHRR error characteristics are not the same. In this region, the set of in situ data are dominated by SSTs from ships. Reynolds et al. (2002) examined the differences between collocated ship and buoy data for a 1982-2000 period between 20°N and 60°N and found a seasonal dependent bias of the ship data with respect to the buoy data which ranged between 0.27°C and 0.11°C. Thus, the bias correction needed for both TMI and AVHRR in the North Pacific may be due to the dominance of ship data there. However, it is difficult to pursue this problem because bias corrections using only buoy data are not accurate in this region because open ocean buoy data are sparse.

7.3 Tropical cyclones

7.3.1 Intensity forecasting

While prediction of hurricane location (track forecasting) has continually improved in the last decade, the prediction of storm strength (intensity forecasting) has not; in fact, forecasts of intensity can still have large errors. The consequences of under or over predicting a storm's strength are significant. On September 16, 1999, Hurricane Floyd hit the US coast, resulting in 57 deaths and estimated total damage of 3 to 6 billion dollars. From September 13th onward, just as the storm was about to make landfall, National Hurricane Center (NHC) intensity models consistently underestimated the storm's magnitude. Conversely, during 2002, a rapid weakening of Hurricane Lili just before landfall was unpredicted by the NHC intensity models, resulting in unnecessary

evacuations. Storm preparation is extremely expensive: depending on population density, evacuation of coastline is estimated 1-50 million dollars per mile (RF), sending the Atlantic naval fleet out to sea for a storm costs an estimated 17 million dollars (RF). Over-estimates of wind speed can result in avoidable costs as unnecessarily large regions are evacuated or the fleet sent to sea, but under-estimates can lead to avoidable property loss, injury, and death. Precise knowledge of the location and strength of winds results in a more precise idea of who and what will be impacted by the storm. Unfortunately, there has be very little improvement in intensity prediction in the last decade. For this reason, improving intensity prediction has been increasingly prioritized.

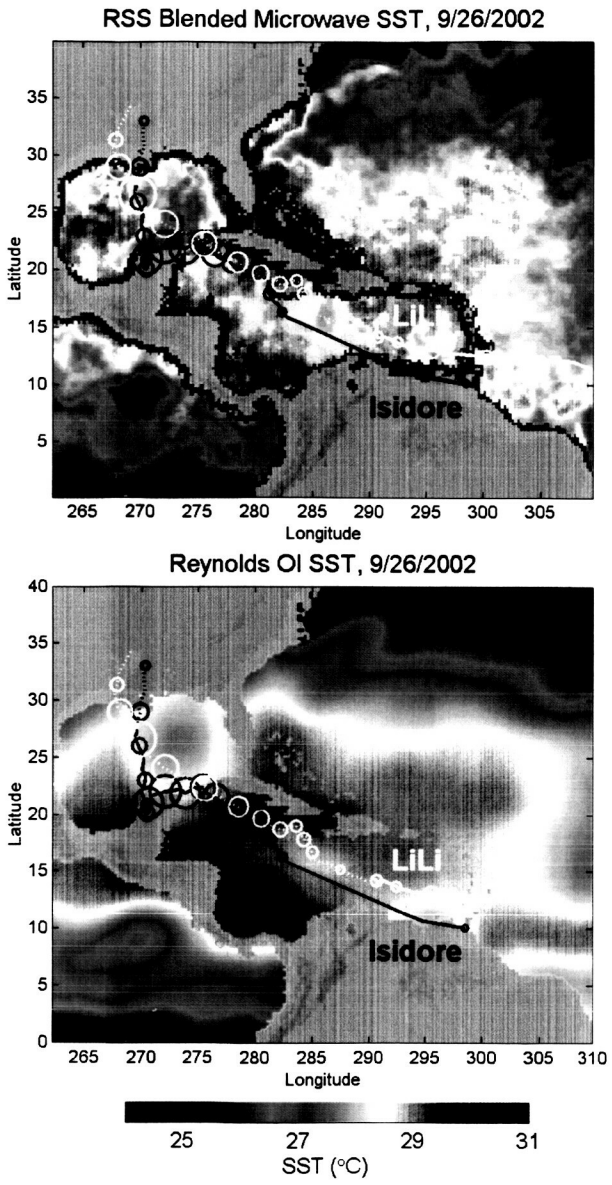

Figure 27. AMSR-E and Reynolds OI SSTs on September 26, 2002. The AMSR-E SSTs show considerably more variability than the smoothed Reynolds OI SSTs. The gray areas adjacent to land in the top figure represent areas where microwave SSTs are not retrieved due to side-lobe contamination. Hurricane Isidore had just passed over the northern Yucatan Peninsula and weakened. The strong winds generated a significant cold wake seen in the AMSR-E SSTs. Hurricane Lili passed over this cold wake, but continued to intensify as it headed towards Louisiana, only weakening just before landfall. These were the two largest storms of the year and both were predicted with less skill than usual.

We have been collaborating with Mark DeMaria at NOAA to examine the effect of daily TMI SSTs on hurricane intensity errors. DeMaria developed the Statistical Hurricane Intensity Prediction Scheme (SHIPS), intensity model which uses climatological, persistence and synoptic predictors. Intensity is predicted using primarily: the difference between the maximum possible intensity (MPI) and current intensity, vertical shear in the atmosphere, persistence, convergence of relative angular momentum, and the zonal wind and temperature within 1000 km of the storm center. MPI is estimated from an empirical relationship between SST and intensity (DeMaria and Kaplan 1994).

Currently, the SHIPS model uses the Reynolds SSTs as an input. We have calculated a microwave optimum interpolated SST (MW OI SST) that includes both TMI and AMSR-E SSTs. Comparison of the Reynolds and MW OI SSTs show that significant temporal and spatial variability is not represented well by the low resolution Reynolds data. A dramatic example of this is

shown in Figure 21, where both Reynolds and MW OI SSTs are plotted on September 26, 2002. Hurricane Isidore had just passed through the Gulf of Mexico with Hurricane Lili following close behind. The Reynolds OI SSTs do not show the cooling North of the Yucatan Peninsula seen in the MW OI SSTs. With Lili following closely, timely knowledge of the oceanic thermodynamic structure was needed for forecasts. In this case, the Reynolds OI SSTs were unable to provide this information to the intensity models. While a storm running over a previous storm's cold wake only occurs perhaps once a year, examining all storms between 1998 and 2000, still shows a correlation between errors in SST and errors in intensity forecasting (Gentemann, 2001).

The value of the MW OI SSTs was tested in the SHIPS hurricane intensity model, run operationally by the National Hurricane Center. SHIPS has skill out to 60 hours using the NCEP weekly 1° optimum interpolated SSTs. Initial results show that using the MW OI SSTs in the intensity model decreased forecast errors and extended skill out to 108 hours. We are currently preparing a paper on this.

7.3.2 Cold wake climatology

Storm reports and summaries issued by the TPC/NHC provide best track position, surface wind speed, and minimum central pressure based on aircraft reconnaissance, satellite measurements, and models for storms in the North Atlantic. Similar reports are issued by the JTWC for global storms. The JTWC best track positions are slightly less accurate as there are less direct measurements. We have taken these storm tracks and created an archive from 1998 through the present of storms overlaid onto TMI optimum interpolated SSTs. An example of one of these images is shown in Figure 28. In addition to the SSTs, we also provide an anomaly map, showing TMI optimum interpolated SSTs minus Reynolds Climatology SST (Figure 29). This allows researchers to quickly browse storms for cold wakes and examine the storm's effect on SSTs. The images have all been processed and we are now working on the web interface.

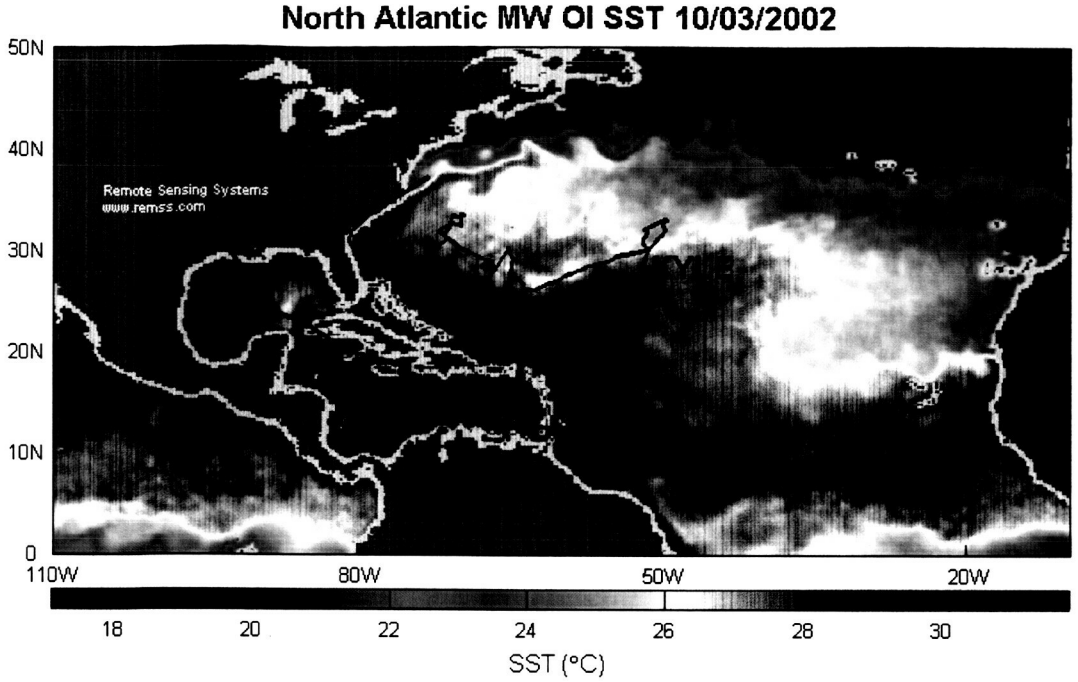

Figure 28. TMI OI SSTs on October 3, 2002. Hurricanes Lili and Kyle were both active in the North Atlantic. Lili is over very warm SSTs. A cold wake can be seen near the track of Kyle.

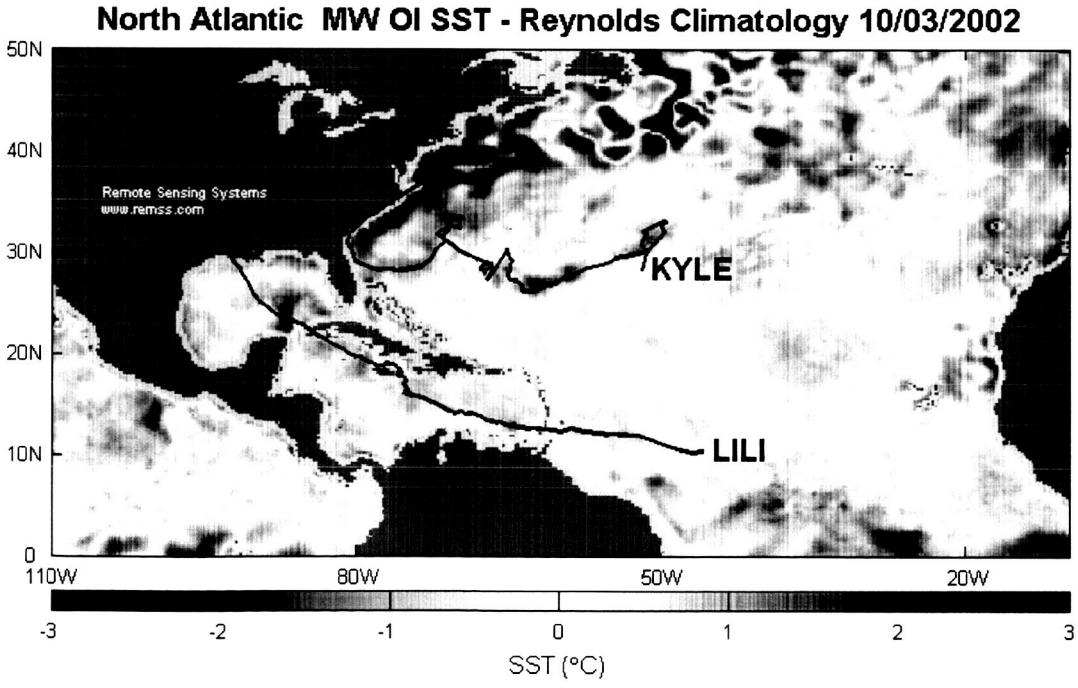

Figure 29. TMI OI SSTs minus Reynolds Climatology on October 3, 2002. The cool wake from Lili and Kyle are clearly seen.

To better examine how storms affect SSTs we are creating an archive of SSTs in the region of storms. The best track positions from the JTWC and NHC are given every three hours. Since the storm translation speed varies, the positions are not equally spaced. First we have taken the best track positions and interpolated a smooth curve onto the track, sampling every 50 km. Next, at each 50 km track location, we interpolated the best estimate of wind speed, minimum pressure, and translation velocity. Finally, we calculated a line perpendicular to the hurricane track, to give us SSTs around the storm. This is shown in Figure 30.

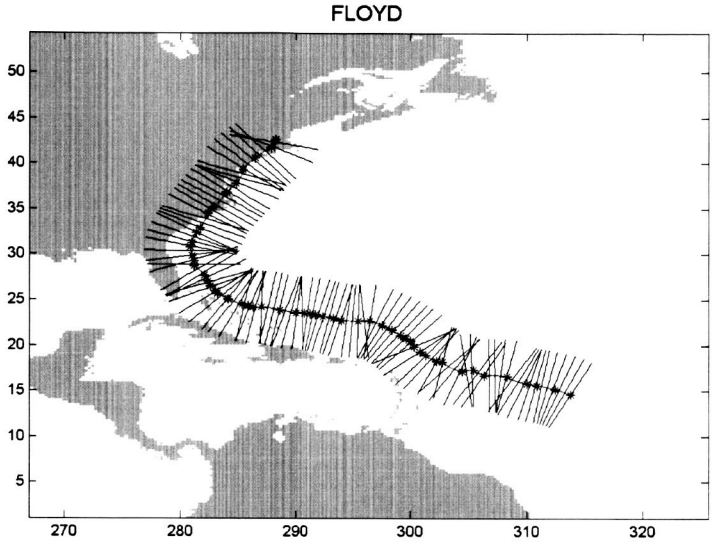

Figure 30. Hurricane Floyd. The NHC best track position is shown by blue dots, the red line is our interpolated position, the black lines are are pendicular to the track, every 50 km.

We are continuing this work by calculating a time series, from five days before the storm to 15 days after storm passage, of SSTs along each of the perpendiculars. This dataset allows us to easily examine both pre-storm conditions and post-storm cold wakes. We now have a complete climatology of SSTs during storms. The SSTs along each tangent, for each point along the storm track, are shown in Figure 31. To better examine post-storm cold wakes, SSTs the day before the storm passage are subtracted from SSTs five days after storm passage.

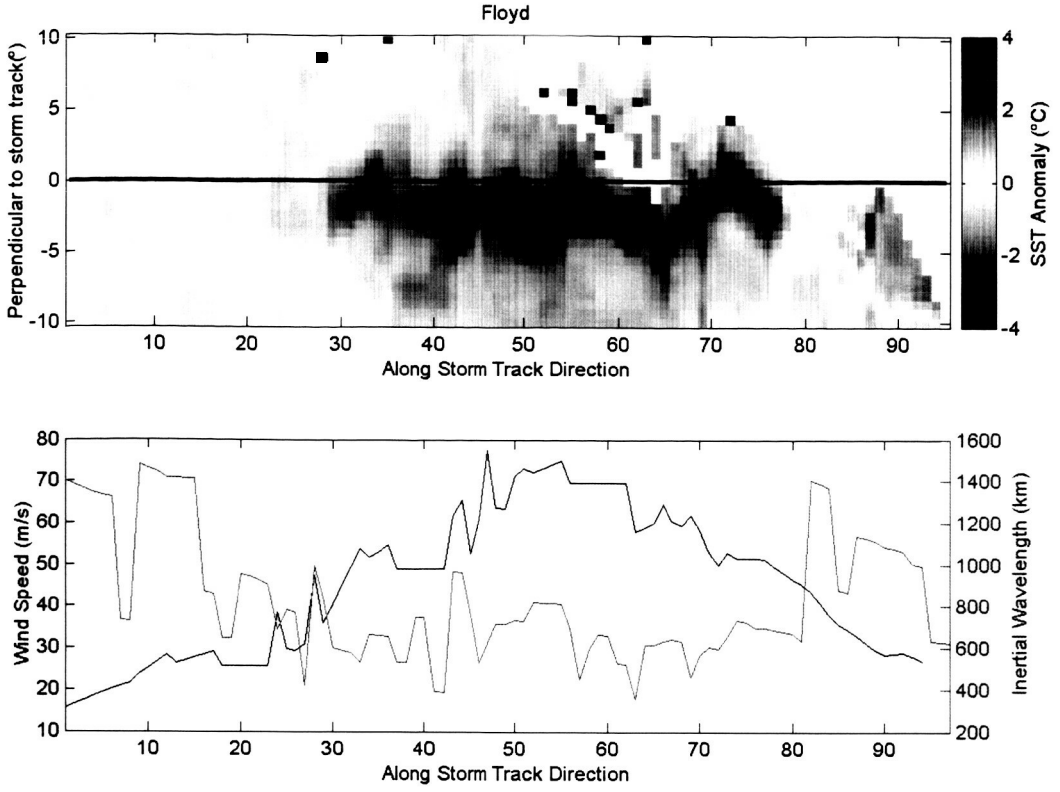

Figure 31. SST after a storm passage. The top figure shows Hurricane Floyd's cold wake. The SST anomaly is calculated as SSTs 5 days after the storm minus SSTs 1 day before the storm. The white in the upper right corner is land mass. The SSTs shown here are calculated along each perpendicular to the storm track, as shown in Figure 30. The bottom figure shows the along track wind speed (blue line) and inertial wavelength (green line). The strong upwelling correlates to the higher wind speeds, and the inertial oscillations seen in the cold wake are smaller, but roughly correlate to the ~650 km wavelength.

Examining SSTs before and after storm passage can help understand the air-sea heat flux during hurricanes, which is very important for understanding air-sea heat transfer processes and predicting storm intensity. This is complicated by the generation of inertial currents in the ocean by the sudden wind changes as a storm passes by. In Figure 31, the storm is traveling down the center of the image, on the black line, from left to right. The right side of the storm is located below the black line, the left side of the storm above the black line. This figure clearly shows the cold wake is much larger on the right side of the storm, where winds are strongest (storm wind velocity plus forward translation velocity). Also, there are fluctuations present in the cold wake. This oscillation is due to upwelling/down welling cycle of inertial oscillations driven by the storm winds. These are slightly less (about 440 km wavelength) than the predicted inertial wavelength, (650 km) which is the product of the storm translation speed and the inertial period at that latitude. We are continuing research in this area.

8 List of Publications Utilizing TRMM data produced by Remote Sensing Systems

Basili, P., P. Ciotti, G. d'Auria, F.S. Marzano and N. Pierdicca (1994). "Use of spaceborne multispectral microwave radiometry for precipitation remote sensing", *Alta Frequenza, 6(6)* 109-111.

Cailliau, D. and V. Zlotnicki (1999). "Precipitation detection by the TOPEX/Poseidon dual-frequency radar altimeter, TOPEX microwave radiometer, Special Sensor Microwave/Imager and climatological ship reports." *IEEE Transactions on Geoscience and Remote Sensing*, in press.

Chelton, D. B., S. K. Esbensen, et al. (2001). "Observations of coupling between surface wind stress and sea surface temperature in the eastern tropical Pacific." *Journal of Climate,* in press.

Chelton, D. B., F. J. Wentz, et al. (2000). "Microwave SST observations of transequatorial tropical instbility waves." *Geophysical Research Letters*, 27(9): 1239-1242.

Chen, C.-T., E. Roeckner, et al. (1996). "A comparison of satellite observations and model simulations of column-integrated moisture and upper-tropospheric humidity." *Journal of Climate,* 9(7): 1561-1585.

Cronin, Meghan F., S-P Xie, and H. Hashzume. (2003). "Barometric pressure variations associated with eastern Pacific tropical instability waves", *Journal of Climate*, 16: 3050-3057.

Gentemann, C. L., C. J. Donlon, et al. (2003). "Diurnal signals in satellite sea surface temperature measurements." *Geophysical Research Letters*, **30**(3): 1140.

Gentemann, C. L., F. J. Wentz, et al. (2003). "In Situ Validation of TRMM microwave sea surface temperatures." Unpublished.

Gentemann, C. L. and F. J. Wentz (2001). "Satellite Microwave SST Accuracy, Comparisons to AVHRR and Reynolds SST, and Measurement of Diurnal Thermocline Variability." Proceedings of the International Geophysics and Remote Sensing Symposium **I**: 246-248.

Goddard Space Flight Center, (2003) "El Nino, The Usual Suspect?" Top story webpage with animations, http://www.gsfc.nasa.gov/topstory/2003/0131nao.html. RSS-supplied data has also been used on various NASA-TV programs.

Jones, C., P. Peterson, et al. (1997). Satellite data estimation of ocean latent heat flux; A neural network approach. 13th Conference on Hydrology, Long Beach, CA, American Meteorological Society.

Kawai, Yoshimi and Hiroshi Kawamura, (2002). Evaluation of the Diurnal Warming of Sea Surface Temperatures Using Satellite-Derived Marine Meteorological Data, *Journal of Oceanography*, 58 (6), 805-814.

Kotroni, Vassiliki, et. al., (2001). The effect of the island of Crete on the Etesian winds over the Aegean Sea, *Quarterly Journal of the Royal Meteorological Society, 127(576),* 1917.

Kubota, M., N. Iwasaka, S. Kizu, M. Konda and K. Kutsuwada, (2002). Japanese ocean flux data sets with use of remote sensing observations (J-OFURO), *J. Oceanogr.*, 58, 213-225.

Kubota, M., H. Muramatsu, et al. (2001). Intercomparison of various surface turbulent heat flux fields. WCRP/SCOR Workshop on Intercomparison and Validation of Ocean-Atmosphere Flux Fields, Bolger Center, Potomac, MD, World Climate Research Program.

Kumar, R. and et al. (1997). "Annual and interannual variation of precipitation over the tropical Indian Ocean." *Journal of Geophysical Research,* **102**(C8): 18519-18527.

Kummerow, C., W. Barnes, et al. (1998). "The tropical rainfall measuring mission (TRMM) sensor package." *Journal of Atmospheric and Oceanographic Technology,* **15**(3): 809-817.

Liu, W. T., W. Tang, et al. (1998). "Spaceborne sensors observe various effects of anomalous winds on sea surface temperatures in the Pacific Ocean." *EOS, Transactions, American Geophysical Union* **79**: 249, 252.

Liu, W. T., A. Zheng, et al. (1994). "Evaporation and solar irradiance as regulators of the seasonal and interanual variablities of sea surface temperature." *Journal of Geophysical Research,* **99**: 12623-12637.

MacKay, Scott and J. Fried. (2003). "The impact of water-velocity variations on deepwater seismic data." *The Leading Edge.* **22**:4.

Martin, Seelye, (2003). *An Introduction to Ocean Remote Sensing.* Cambridge: Cambridge University Press.

Nakai, S., (2000). Regional difference of relation between upper-level cloud area and precipitable water content. Proceedings, the 13th International Conference on Clouds and Precipitation, 14-18 August 2000, Reno, Nevada, USA, 1173-1176.

Nakai, S., K. Nakamura, H. Minda and H. Seko, (2001). A mesoscale cloud cluster over the East China Sea detected by TRMM and an aircraft dropsonde observation (in Japanese with English abstract). *Rep. Natl.Res. Inst. Earth Sci. Disast. Prev.*, No. 61, 93-106.

Otterman, J., D. Starr, R. Atlas, J. Ardizzone, and J. Terry, (1998). Space observations of ocean surface winds aid monitoring of Northeast Pacific climate shifts, *Eos, Transactions, American Geophysical Union, 79* (47), 575-581.

Prasad, V.S., (2002). Impact of high resolution satellite wind vector data on NCMRWF assimilation and forecasting system, *Mausam, 54*, 237-246.

Rajeevan, M., (2001). Asymmetric thermodynamic structure of monsoon depression revealed in microwave satellite data, *Current Science 81(5),* 448-450.

Ricciardulli, L. and F. J. Wentz, (2003). "Insights Gained from a TRMM Microwave and Infrared Sea Surface Temperature Comparison." Proceedings of the Oceans 2003 Conference, 22-26 September 2003, San Diego, California, 1839-1842.

Ricciardulli, L. and F. J. Wentz, (2003). "Errors and Uncertainties in Sea Surface Temperature Retrievals from Space by Comparison of Microwave and Infrared Observations from TRMM", manuscript in preparation.

Sajith V, K.R. Santosh, and H.S. Ram Mohan, (2003). Intraseasonal Oscillation of Total Precipitable Water over North Indian Ocean and its application in the diagnostic study of coastal rainfall, *Geophys. Res. Lett*, 30(20), 2054, doi:10,1029/2003GL017635.

Santer, B. D., T. M. L. Wigley, et al. (2003). "Influence of Satellite Data Uncertainties on the Detection of Externally Forced Climate Change." *Science* **300**: 1280-1284.

Schluessel, P. and A. Albert (1999). "Latent heat flux at the sea surface retrieved from combined TMI and VIRS measurements of TRMM." *to be submitted.*

Vazquez, J., R. M. Sumagaysay, et al. (1999). NOAA/NASA AVHRR Oceans Pathfinder Sea Surface Temperature Data Set User's Reference Manual. Pasadena, California, Jet Propulsion Laboratory.

Vecchi, Gabriel A. and D. E. Harrison, (2002). Monsoon breaks and subseasonal sea surface temperature variability in the Bay of Bengal, *Journal of Climate 15(12)* 1485-1493.

Wentz, F., C. Gentemann, et al. (2000). "Satellite measurements of sea surface temperature through clouds." *Science*, **288**(5467): 847-850.

Wentz, F. J. and M. Schabel (2000). "Precise climate monitoring using complementary satellite data sets." *Nature*, **403**(6768): 414-416.

Wentz, F. J., P. D. Ashcroft, et al. (2001). "Post-launch calibration of the TMI microwave radiometer." IEEE Transactions on Geoscience and Remote Sensing **39**(2): 415-422.

Wood, R. et. al., (2002). Diurnal cycle of liquid water path over the subtropical and tropical oceans, *Geophysical Research Letters,* 10.1029/2002GL015371.

REPORT DOCUMENTATION PAGE

Form Approved
OMB No. 0704-0188

1. AGENCY USE ONLY *(Leave blank)*	2. REPORT DATE	3. REPORT TYPE AND DATES COVERED
	October 28, 2003	Final Technical Report, October 2000-September 2003

4. TITLE AND SUBTITLE
Sensor Calibration and Ocean Products for TRMM Microwave Radiometer
Final Technical Report

5. FUNDING NUMBERS
NAS5-00217

6. AUTHORS
Frank J. Wentz

7. PERFORMING ORGANIZATION NAME(S) AND ADDRESS(ES)
Remote Sensing Systems
438 First Street, Suite 200
Santa Rosa, CA 95401

8. PERFORMING ORGANIZATION REPORT NUMBER
102803

9. SPONSORING/MONITORING AGENCY NAME(S) AND ADDRESS(ES)
NASA
Goddard Space Flight Center
Greenbelt, MD 20771

10. SPONSORING/MONITORING AGENCY REPORT NUMBER

11. SUPPLEMENTARY NOTES

12a. DISTRIBUTION/AVAILABILITY STATEMENT
no restrictions

12b. DISTRIBUTION CODE

13. ABSTRACT *(Maximum 200 words)*

During the three years of funding, we have carefully corrected for two sensor/platform problems, developed a physically based retrieval algorithm to calculate SST, wind speed, water vapor, cloud liquid water and rain rates, validated these variables, and demonstrated that satellite microwave radiometers can provide very accurate SST retrievals through clouds. Prior to this, there was doubt by some scientists that the technique of microwave SST retrieval from satellites is a viable option. We think we have put these concerns to rest, and look forward to making microwave SST's a standard component of the Earth science data sets. Our TMI SSTs were featured on several network news broadcasts and were reported in Science magazine.

Additionally, we have developed a SST algorithm for VIRS to facilitate IR/MW inter-comparisons and completed research into diurnal cycles and air-sea interactions.

14. SUBJECT TERMS
sea-surface temperature, satellite microwave radiometry

15. NUMBER OF PAGES
45

16. PRICE CODE

17. SECURITY CLASSIFICATION OF REPORT	18. SECURITY CLASSIFICATION OF THIS PAGE	19. SECURITY CLASSIFICATION OF ABSTRACT	20. LIMITATION OF ABSTRACT
unclassified	unclassified	unclassified	UL